MASTERARBEIT / MASTER'S THESIS

Titel der Masterarbeit / Title of the Master's Thesis

Dynamical Friction in FDM Halos

verfasst von / submitted by

Frank Schindler, BSc

angestrebter akademischer Grad / in partial fulfillment of the requirements for the degree of

Master of Science (MSc)

Wien, 2023 / Vienna, 2023

Studienkennzahl lt. Studienblatt / degree programme code as it appears on the student record sheet:	UA 066 876
Studienrichtung lt. Studienblatt / degree programme as it appears on the student record sheet:	Masterstudium Physics
Betreut von / Supervisor:	Univ.-Prof. Piotr T. Chruściel, MSc PhD
Mitbetreut von / Co-Supervisor:	Mateja Gosenca, MSc PhD

Abstract

In this thesis we perform a detailed exploration of the dynamics of massive objects in a fuzzy dark matter (FDM) halo. FDM is a dark matter candidate composed of very light bosons ($m_b \sim 10^{-22}$ eV) and modeled by the Schrödinger-Poisson equations. We simulate the gravitational dynamics of a point mass interacting with FDM using AxioNyx. The studied scenarios have at least two physical applications. A very massive test objects applies to the physical scenario of a supermassive black hole orbiting close to a galactic center, while less massive test objects are comparable to massive stars moving in a halo. We reproduce previous results for a point mass orbiting and inspiraling in an FDM soliton to verify our numerical methods. In these simulations we confirm the solitonic oscillation frequency formula, the rough estimates of orbital lifetimes and also observe that the inspiral may get reversed by solitonic oscillations. We then perform first simulations of a point mass orbiting inside an FDM halo consisting of a solitonic core surrounded with order-one density fluctuations. This scenario is relevant for example for the first phase of massive binary black hole mergers driven by dynamical friction. From our simulations we estimate the order of magnitude of the effective mass of the stochastic density fluctuations ("granules"), which is a crucial quantity for the relaxation in FDM. Furthermore, we explore the parameter space of the point mass, starting radius, as well as the FDM boson mass m_b. Our results clearly show that even relatively massive test objects (10^7 $M_\odot$) do not sink towards the central soliton but stop inspiraling at some distance from the center of mass. The stalling distance agrees with the approximate theoretical prediction for the stalling radius.

Zusammenfassung

In dieser Arbeit untersuchen wir detailliert die Dynamik massiver Objekte in einem "fuzzy dark matter" (FDM) Halo. FDM ist ein aus extrem leichten Bosonen ($m_b \sim 10^{-22}$ eV) bestehender Kandidat für Dunkle Materie. Mathematisch wird FDM mit den Schrödinger-Poisson Gleichungen beschrieben. Wir simulieren die Gravitationsdynamik einer mit FDM interagierender Punktmasse mit AxioNyx. Die hier untersuchten Szenarien haben zumindest zwei verschiedene physikalische Anwendungen. Eine sehr massereiche Punktmasse entspricht dem physikalischen Szenario eines supermassiven schwarzen Lochs im Orbit eines galaktischen Halos, während kleinere Punktmassen vergleichbar mit Sternen sind. Wir reproduzieren vorherige Ergebnisse für eine Punktmasse im Orbit in einem FDM Soliton, um unsere numerische Methoden zu verifizieren. In diesen Simulationen prüfen wir auch die Formel für die Frequenz der Soliton-Oszillationen, die grobe Schätzungen für orbitale Lebensdauer und beobachten, dass durch Einwirken der solitonischen Oszillationen die Orbits der Punktmassen nicht monoton sinken. Danach durchführen wir die ersten Simulationen von Punktmassen im Orbit in einem FDM Halo, bestehend aus einem Soliton Kern umgeben von Dichteschwankungen. Dieses Szenario ist relevant zum Beispiel für die erste Phase der Verschmelzung zweier Schwarzer Löcher, da sie durch Dynamische Reibung angetrieben wird. Aus unseren Simulationen schätzten wir die Größenordnung der effektiven Masse der stochastischen Dichteschwankungen (engl. "granules"), welche für die Relaxation in FDM eine wichtige Größe darstellt. Weiters haben wir den Parameterbereich für die Punktmasse, den Anfangsradius und die FDM Boson Masse m_b untersucht. Unsere Ergebnisse zeigen, dass sogar relativ schwere Testmassen (10^7 $M_\odot$) nicht ganz bis zum zentralen Soliton sinken und der Orbit stabilisiert sich bei einer Entfernung von dem Massenzentrum. Die Entfernung entspricht mit den theoretischen Vorhersagen für den sogenannten "stalling radius".

Acknowledgements

I would like to thank my supervisor Mateja Gosenca for suggesting this topic, for her guidance and patience, and for many helpful discussions during the time of writing this thesis. Furthermore I would like to thank my parents for their support.
The computational results presented in this work have been performed using the Vienna Scientific Cluster (VSC).

Contents

1 Introduction

1.1 Motivation for dark matter

In the current concordance model of the universe (also called ΛCDM model), the energy-density of the universe consists of 3 main components: about 69 % is dark energy and about 26 % is dark matter and about 5 % is baryonic matter (e.g. see [2]). The value for the baryonic matter density is consistent throughout multiple independent observations like the measurements of the Cosmic microwave background (CMB) or measurements of abundance of helium and deuterium in the universe, which agree that baryonic matter composes around 5% of the energy density of the universe. At the same time observations of anisotropies in the CMB or observations of weak gravitational lensing and galaxy clustering agree that in total about 30 % of the energy density of the universe is composed of matter (e.g. see Table 2 in [1]). Therefore dark matter seems to be necessary to make up the difference [3]. Galaxy rotation curves also provide independent observations which hint at the existence of dark matter (e.g. [4]). In summary, there are plenty of independent observations which can all be explained by the existence of dark matter.

1.2 Fuzzy dark matter

Despite an abundance of evidence supporting the existence of dark matter, its exact nature is unknown. Based on current observations, dark matter is expected to have the following properties [3]: 1.) nonrelativistic, 2.) noncollisional and 3.) noninteracting[1] with radiation and "visible" matter. One model with these properties is the so-called "cold dark matter" (CDM). Concrete proposed candidates that have these qualities include thermal weakly interacting massive particles (WIMPs), massive compact halo objects (MACHOs) and primordial black holes. In this thesis we will focus on another dark matter candidate called "fuzzy dark matter" (FDM) consisting of ultralight bosonic particles. In literature FDM is sometimes also referred to as "scalar field dark matter","wave(like) dark matter" (e.g. in [5]) or ultralight dark matter (ULDM) and has been studied as a dark matter candidate for quite some time now (e.g. in [6] published in 2000). The dynamics of FDM is described by the Schrödinger-Poisson equations and on length scales larger than the de Broglie wavelength its behavior matches that of CDM. At scales comparable to the de Broglie wavelength new phenomena arise due to additional wave-like effects.

Simulations of the universe using CDM lead to predictions which on large scales are in good agreement with the observations of the universe but on smaller scales some notable discrepancies arise [7], [6]: (a) The CDM model predicts more small satellite galaxies than are observed. (b) CDM predicts more massive satellite galaxies that should contain stars than are observed. (c) The central density profiles of many observed low-mass systems are flat, whereas CDM predicts NFW cusps ("core-cusp problem"). These discrepancies in general point out that using CDM as the model for dark matter leads to an overabundance of structure on small scales in simulations. FDM does not suffer from these problems, since structure formation on small scales is suppressed by FDM and it has a stable soliton solution, that has been shown in simulations to be at the core of

[1] Other than gravitationally.

FDM halos [5]. The soliton density profile is much flatter in the center than the NFW profile predicted by CDM, which alleviates the "core-cusp problem".

In many galaxies black holes can be found near the center of the galaxies and the centers themselves usually contain a supermassive black hole (SMBH). These SMBHs are usually products of mergers of smaller black holes that themselves were at the centers of smaller galaxies that merged together to form a bigger galaxy. The evolution of massive black hole (MHB) binaries consists of 3 phases [8]. The first phase starts when galaxies merge and their MBHs sink towards the center of the new galaxy due to dynamical friction where they form a binary. After that in the second phase the binary will continue to decay up to a point when the emission of gravitational waves becomes efficient at carrying away the angular momentum of the black holes. This point is the start of the final third phase and the actual processes that bring the binary MBHs close enough to kick of phase three are poorly understood [11]. This problem is known in literature as the "final parsec problem" [8]. With that in mind, it is useful to study whether FDM can alleviate or exacerbate this problem.

To study the effects of dynamical friction on massive test objects in orbit inside an FDM halo, we will perform numerical simulations of scenarios where a point mass is in orbit inside an FDM halo. The effects of dynamical friction on test masses in FDM have been theoretically studied for example in [9], [10] as well as in numerical simulations such as presented in [11]. This work goes beyond the simulations in [11] in the second part by simulating test masses orbiting inside FDM halos. For this we also used adaptive mesh refinement, since we have to simulate a large volume to reduce the effects from periodic boundary conditions and the point mass trajectory is only confined to a small region of the whole simulation volume.

1.3 Outline of this work

This thesis is structured in the following way: In Chapter 2 a literature review of FDM is given with a focus on the results most relevant for this thesis like the soliton solution, FDM halos and an overview of current constraints on the mass of a hypothetical FDM particle. Chapter 3 provides an overview of the theory of relaxation in FDM. Chapter 4 describes the numerical methods used in the simulations as well as the initial conditions used to set up our simulations. In Chapters 5 and 6 the results of our simulations are presented. In Chapter 5 we show results of simulations of a test mass orbiting in a soliton while in Chapter 6 the results of more computationally heavy simulations with test masses orbiting in an FDM halo are presented.

1.4 Preliminaries

Candidate particles for FDM are hypothetical bosons with very small masses in the range around 10^{-22} eV. This range is being investigated because the additional quantum effects from FDM become significant at length scales around the de Broglie wavelength $\lambda_{dB} = \frac{h}{m_b v}$ and below (h is the Planck's constant). For example taking $\lambda_{dB} = 100$ pc (distances on this scale are relevant at when studying galaxies) and $v = 100$ km/s (typical order of magnitude of velocities of stars) for the velocity corresponds to $m_b = 10^{-22}$ eV. So quantum effects get relevant on astrophysical scales for a hypothetical boson with a mass in this range. Since λ_{dB} is inversely proportional to m_B, for large enough masses λ_{dB} becomes too small for FDM to be distinguishable from CDM. For more details about constraints from observations on the mass of a hypothetical FDM particle see the section 1.10.

1.4.1 Action of axion-like particles

In this section we show how to derive the equations describing fuzzy dark matter from the assumption that it consists of axion-like particles (ALPs). We start with a real scalar field ϕ that satisfies the Klein-Gordon equation and work with units such that $\hbar = c = 1$. Then the action S linked to ALPs is written as the action of a scalar field given by (for more details see [12], [7])

$$S = S_{EH} + S_\phi = \int d^4x \sqrt{-g}\left(\frac{\mathcal{R}}{16\pi G} + \mathcal{L}_\phi\right) \tag{1.1}$$

where S_{EH} is the Einstein-Hilbert action with g being the determinant of the metric tensor, $\mathcal{R}$ being the Ricci scalar and G being Newton's constant of gravity. The Lagrangian density $\mathcal{L}_\phi$ is defined as

$$\mathcal{L}_\phi = \frac{1}{2} g^{\mu\nu} \partial_\mu \phi \partial_\nu \phi - V(\phi) \tag{1.2}$$

with $g^{\mu\nu}$ being the metric tensor and $V(\phi)$ the potential which acts on the field ϕ. Here m_b is the mass of the ALP. For our purposes it is appropriate to work in the Newtonian gauge and consider only scalar perturbations to the FLRW metric:

$$g_{00} = -1 + 2\Phi(\mathbf{x}, t), \qquad g_{0i}(\mathbf{x}, t) = 0, \qquad g_{ij}(\mathbf{x}, t) = a^2(t)\delta_{ij}[1 + 2\Phi(\mathbf{x}, t)]. \tag{1.3}$$

In our notation a is the cosmic scale factor and Φ is the gravitational potential. In this gauge (when keeping terms up to first order of the potential and up to second order of the spatial derivatives of the potential) S_{EH} simplifies [12] to

$$S_{EH} = \int d^4x\ a^3 \left[-\frac{(\partial_i \Phi)^2}{8\pi G a^2} - (2\langle\dot{\phi}^2\rangle - m_b^2 \langle \phi^2 \rangle)\Phi \right] \tag{1.4}$$

where dot denotes the time derivative. Meanwhile the quadratic form of S_ϕ is

$$S_\phi = \int d^4x\ a^3 \left[\frac{1}{2}(1 - 4\Phi)\dot{\phi}^2 - \frac{1}{2a^2}(\partial_i \phi)^2 - (1 + 2\Phi)V(\phi) \right]. \tag{1.5}$$

For the potential $V(\phi)$ one takes $V(\phi) = \frac{1}{2} m_b^2 \phi^2$. Next, we write ϕ as

$$\phi = \frac{1}{\sqrt{2m_b a^3}} (\psi e^{-im_b t} + \psi^* e^{im_b t}) \tag{1.6}$$

with ψ being a complex field. Then after making some simplifying assumptions (like $\dot{\psi} \ll m_b \psi$, $\dot{a} \ll a m_b$) and neglecting terms containing powers of $e^{\pm i m_b t}$. In this case the action (1.1) becomes

$$S = \int d^4x \left[\frac{i}{2}(\dot{\psi}\psi^* - \psi\dot{\psi}^*) - \frac{(\partial_i \psi)(\partial_i \psi^*)}{2m_b a^2} - m_b(\psi\psi^* - \langle\psi\psi^*\rangle)\Phi - \frac{a}{8\pi G}(\partial_i \Phi)^2 \right]. \tag{1.7}$$

1.4.2 Equations of motion

In the remainder of this thesis, unless stated otherwise, we will work in a static background and therefore take $a = 1$ in our equations. With that one gets from (1.7) the following Lagrangian $\mathcal{L}$

$$\mathcal{L} = -\frac{1}{8\pi G}|\nabla\Phi|^2 - m_b\Phi(|\psi|^2 - \langle|\psi|^2\rangle) - \frac{1}{2m_b}|\nabla\psi|^2 + \frac{i}{2}(\dot{\psi}\psi^* - \psi\dot{\psi}^*). \tag{1.8}$$

Next we calculate the Euler-Lagrange equations of motion using the following relation:

$$|\nabla\psi|^2 = \nabla(\psi^*\nabla\psi) - \psi^*\nabla^2\psi.$$

The equation of motion for ψ^* is (with $\hbar$ restored)

$$i\hbar\dot{\psi} = -\frac{\hbar^2}{2m_b}\nabla^2\psi + m_b\Phi\psi \tag{1.9}$$

which is the Schrödinger equation for a field consisting of particles of mass m_b. Meanwhile the equation of motion for Φ is

$$\nabla^2\Phi = 4\pi G m_b(|\psi|^2 - \langle|\psi|^2\rangle) \tag{1.10}$$

which is the Poisson equation for a gravitational potential Φ and $|\psi|^2 = m_b\rho$ is the density of the field. Together, these two equations are known in literature as the Schrödinger-Poisson system and the FDM model considered in this thesis is modeled by this system. A solution ψ to this system of equations is a scalar field consisting of bosons with mass m_b. The subtracted term $\langle|\psi|^2\rangle$ is the background density, which does not contribute to the gravitational force.

1.5 Madelung equations

There is an alternative equivalent formulation of the Schrödinger equation in terms of hydrodynamical variables, which can be derived after applying the so-called Madelung transformation [12] to the wavefunction and writing it as

$$\psi = \sqrt{\frac{\rho}{m}}e^{im_b\theta/\hbar}. \tag{1.11}$$

Note that the quantity $\mathbf{v} = \frac{\hbar}{m_b}\nabla\theta$ corresponds to the flow velocity. With the Madelung transformation the Schrödinger equation (1.9) may be rewritten and after splitting the real and imaginary parts one eventually gets the so-called "Madelung equations" [12]:

$$\partial_t\rho + \nabla(\rho\mathbf{v}) = 0 \qquad \text{and} \qquad \partial_t\mathbf{v} + (\mathbf{v}\nabla)\mathbf{v} = -\nabla\Phi + \frac{\hbar^2}{2m_b^2}\nabla\left(\frac{\nabla^2\sqrt{\rho}}{\sqrt{\rho}}\right). \tag{1.12}$$

These equations are analogous to mass and momentum conservation equations of fluid dynamics. The last equation contains the contribution of "quantum pressure" Q defined as

$$Q = -\frac{\hbar^2}{2m_b^2}\frac{\nabla^2\sqrt{\rho}}{\sqrt{\rho}}. \tag{1.13}$$

The appearance of this term in the second equation is the only difference between these equations and the usual Euler equations of fluid dynamics. Importantly, this term is responsible for the interference patterns in FDM systems.

One can use these equations to estimate the length scales at which quantum effects become significant and therefore where FDM should differ from CDM. Consider a spherical halo of mass M and radius R [12]. We compare the velocity term on the left-hand side of the second equation of (1.12) with the quantum pressure term by considering the ratio of Q and v^2 ($v = |\mathbf{v}|$). The Q term roughly scales as R^{-2} so one gets

$$\frac{Q}{v^2} \sim \frac{\hbar^2}{m_b^2 R^2} \frac{1}{v^2} = \left(\frac{\lambda\!\!\!^{-}_{dB}}{R}\right)^2 \tag{1.14}$$

with $\lambda\!\!\!^{-}_{dB} = \frac{\hbar}{m_b v}$ being the reduced de Broglie wavelength. From this result one can conclude that FDM will behave like CDM on length scales R when $R \gg \lambda\!\!\!^{-}_{dB}$, since the contribution from quantum pressure will be small. However the quantum pressure term will become relevant on length scales below $\lambda\!\!\!^{-}_{dB}$.

1.6 Dimensionless form of the Schrödinger-Poisson system

To simplify the numeric implementation we will recast the Schrödinger-Poisson equations into a dimensionless form. Firstly, we will rescale time, position, gravitational potential and the wavefunction in the same way as in [13], i.e.

$$\tilde{t} = \frac{t}{\mathcal{T}}, \qquad \tilde{\mathbf{x}} = \frac{\mathbf{x}}{\mathcal{L}}, \qquad \tilde{\Phi} = \frac{m_b \mathcal{T}}{\hbar}\Phi, \qquad \tilde{\psi} = \mathcal{T}\sqrt{m_b G}\psi \tag{1.15}$$

with the following constant factors ($H_0 \approx 67.5$ km s^{-1} Mpc^{-1} is the present day Hubble constant and $\Omega_{m_0} \approx 0.31$ is the present day matter density fraction of the universe energy density)

$$\mathcal{L} = \left(\frac{8\pi\hbar^2}{3m_b^2 H_0^2 \Omega_{m_0}}\right)^{1/4} \approx 121\left(\frac{10^{-23}\,\mathrm{eV}}{m_b}\right)^{1/2} \mathrm{kpc}$$

$$\mathcal{T} = \left(\frac{8\pi}{3H_0^2 \Omega_{m_0}}\right)^{1/2} \approx 75.5\ \mathrm{Gyr} \tag{1.16}$$

$$\mathcal{M} = \frac{1}{G}\left(\frac{8\pi}{3H_0^2 \Omega_{m_0}}\right)^{-1/4} \left(\frac{\hbar}{m_b}\right)^{3/2} \approx 7 \cdot 10^7 \left(\frac{10^{-23}\,eV}{m_b}\right)^{3/2} \mathrm{M}_\odot.$$

Inserting the new variables into (1.9) and using the fact that $\frac{\hbar}{m_b}\frac{\mathcal{T}}{\mathcal{L}^2} = 1$ gives

$$i\dot{\psi} = -\frac{1}{2}\nabla^2\psi + \Phi\psi. \tag{1.17}$$

Inserting the new variables into the Poisson equation (1.10) and using $\frac{m_b}{\hbar}\frac{\mathcal{L}^2}{\mathcal{T}^2} = 1$ gives

$$\nabla^2\Phi = 4\pi(|\psi|^2 - \langle|\psi|^2\rangle). \tag{1.18}$$

This equations are now dimensionless and to restore the correct dimensions for the density we will have to do the following

$$\rho = \frac{\mathcal{M}}{\mathcal{L}^3}|\psi|^2. \tag{1.19}$$

To get the mass inside the volume V we take

$$M = \mathcal{M} \oint_V d^3x|\psi|^2. \tag{1.20}$$

So $\mathcal{L}, \mathcal{M}, \mathcal{T}$ are the factors needed to recover the dimensions of mass, length and time. In the following we use the dimensionless quantities from (1.15) but drop the tilde from the notation.

1.7 Soliton solution

The soliton solution is a spherically symmetrical, stationary and stable solution to the Schrödinger-Poisson system given by (1.9) and (1.10) . It will be used a lot throughout this thesis and therefore this section will provide details on how to arrive at this solution, which has to be done numerically. We will work with the dimensionless form of the equations given in the previous section (equations (1.17) and (1.18)).

The solution will have spherical symmetry and the density $\rho(r)$ will not depend on time, so the wavefunction can only have a phase factor depending on t, e.g. ψ and Φ will be of the form

$$\psi(t, \vec{x}) = e^{i\beta t} f(r), \qquad \Phi(t, \vec{x}) = \varphi(r). \tag{1.21}$$

The Laplace operator in spherical coordinates applied to a spherically symmetric function $g = g(r)$ is

$$\Delta^2 g(r) = \frac{1}{r^2}\frac{\partial}{\partial r}\left(r^2 \frac{\partial}{\partial r} g(r)\right).$$

Thus the Schrödinger equation (1.17) with our Ansatz (1.21) becomes

$$i\partial_t(e^{i\beta t} f(r)) = -\frac{1}{2}\frac{1}{r^2}\partial_r(r^2\partial_r(e^{i\beta t} f(r))) + e^{i\beta t} f(r)\varphi(r)$$

which is equivalent to

$$0 = -\frac{1}{2} f''(r) - \frac{1}{r} f'(r) + f(r)\tilde{\varphi}(r). \tag{1.22}$$

Here $\tilde{\varphi}(r) = \varphi(r) + \beta$ .The Poisson equation (1.18) with this Ansatz becomes

$$\frac{1}{r^2}\partial_r(r^2\varphi'(r)) = 4\pi(|e^{i\beta t} f(r)|^2)$$

which is the same as

$$\tilde{\varphi}''(r) + \frac{2}{r}\tilde{\varphi}'(r) - 4\pi f(r)^2 = 0. \tag{1.23}$$

The solution to the system of equations (1.22) and (1.23) is the soliton solution and in the next section a procedure to find the solution numerically is given.

1.7.1 Finding the numerical solution

The system of equations derived in the last section is a second order coupled system of differential equations and to solve it numerically we first need to reduce it to a coupled system of first order equations by introducing new variables:

$$\begin{aligned} x_1(r) &:= f(r), \qquad & x_2(r) &:= f'(r) \\ y_1(r) &:= \varphi(r), \qquad & y_2(r) &:= \varphi'(r) \end{aligned} \tag{1.24}$$

With these variables our system consists of four coupled first order differential equations:

$$\begin{aligned} x_1' &= x_2, \qquad & x_2' &= -\frac{2}{r}x_2 + 2x_1 y_1 \\ y_1' &= y_2, \qquad & y_2' &= -\frac{2}{r}y_2 + 4\pi x_1^2 \end{aligned} \tag{1.25}$$

To solve this system numerically we will use the fourth-order Runge-Kutta method, which in general solves a first order differential equation of the form $g'(r) = z(r, g)$ in the following way:

$$g_{n+1} = g_n + \frac{h}{6}(k_1 + 2k_2 + 2k_3 + k_4) \tag{1.26}$$

with

$$\begin{aligned} k_1 &= z(r_n, g_n) \\ k_2 &= z(r_n + h/2, g_n + k_1 h/2) \\ k_3 &= z(r_n + h/2, g_n + k_2 h/2) \\ k_4 &= z(r_n + h, g_n + k_3 h). \end{aligned} \tag{1.27}$$

Since we have a system of four first-order differential equations, each of them has to be evolved according to (1.26). Furthermore this scheme requires initial values for x_1, x_2, y_1, y_2. We choose the initial value of x_1 to be 1, because as we will later show the solution can be rescaled to any arbitrary positive value. More importantly, the initial value of x_2 has to be 0, because we assume that at the origin the soliton density has a maximum, hence $f'(r = 0) = 0$. Analogously we set y_2 initially to 0, since the gravitational potential should have a minimum at the origin. This leaves us with choosing the initial value of $y_1 = \varphi(r)$, which we cannot choose a priori, but we have to take an initial guess and use a variational method to find the appropriate initial value $y_1(r = 0) = p$. To find p we use the bisection method to vary the value of p in an interval initially set to $[-5, 5]$. The following 2 conditions have to be used to abort the evolution and move on to the next value for p:

1. If for a given p at any given iteration step the value of x_1 would increase, i.e. if $x_1(r_2) > x_1(r_1)$ for any $r_2 > r_1$

2. If at any given iteration step the value of x_1 becomes negative.

This is because we want the density of the solution to be a monotonically decreasing function of r.

Finally we divided the domain of r given as $(0, 8]$ into 10000 uniform intervals with our grid points located at the end of each interval. We implemented the solver using Python with the packages scipy and numpy. With this the code found a solution approximately at $p = -2.3025$. There is no exact analytical formula for the soliton solution, but the literature commonly uses the approximate formula from [5]. This formula comes from a numerical fit for a radius up to 3 times the core radius r_c (defined as the radius at which the density reaches half its initial value) and is given by:

$$\rho_s(r) = \frac{1.9 \cdot (m_b/10^{-23}\text{ eV})^{-2}(r_c/\text{kpc})^{-4}}{(1 + 9.1 \cdot 10^{-2}\ r^2/r_c^2)^8}\ \text{M}_\odot\text{pc}^{-3}. \tag{1.28}$$

To compare the numerical solution obtained by the method described above we have to restore units, which can be done using the factors given in Equation (1.16), e.g. for each dimension of length we multiply with $\mathcal{L}$, for mass with $\mathcal{M}$ etc.. For a mass $m_b = 10^{-23}$ eV the result is shown in Figure 1.1 and on a log scale in the left panel of Figure 1.2. The right panel of 1.2 shows the relative difference between the numerical solution and the formula (1.28) on a log scale to showcase that the difference is generally small and grows only for large radii where the density is anyway very small.

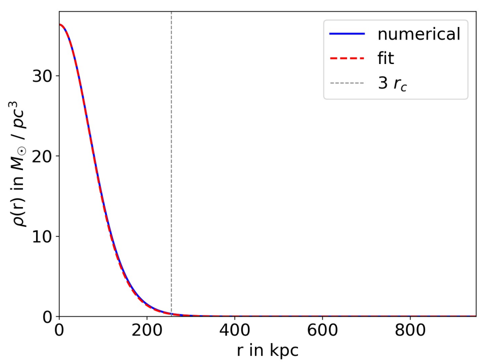

Figure 1.1: The density profile of the numerical soliton solution found by the method described in this section. For comparison the formula (1.28) is plotted. The vertical line is drawn at $3r_c$.

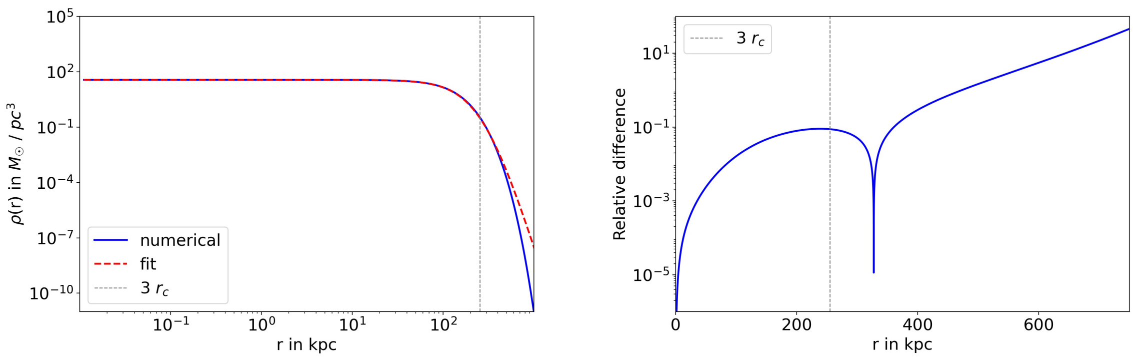

Figure 1.2: Left: Log-Log plot of the soliton density profile and the fit (1.28) for comparison. Right: The relative difference of the numerical solution and the fit from (1.28). The vertical line is drawn at $3r_c$.

We may use the numerical solution which we found and rescale it, since the following scaling relations hold for the solitonic solution [5], [13]:

$$(r, \psi, \rho, M_S) \to (r/\alpha, \alpha^2\psi, \alpha^4\rho, \alpha M_S). \tag{1.29}$$

Here M_S is the total mass of the soliton. It is worth noting that these relations imply that a more massive soliton will be more compact and will have a smaller core radius r_c, i.e. more massive solitons are smaller in size. In Figure 1.3 the density profile of a soliton of a given mass $M_{tot} = 2.68 \cdot 10^8$ M$_\odot$ and that of a rescaled soliton with 1/10 of that mass is plotted.

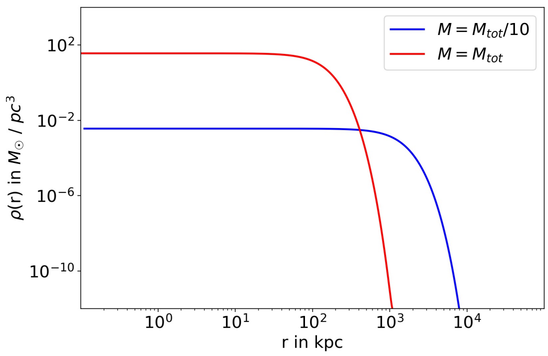

Figure 1.3: Red: Numerical soliton solution for a given total mass $M_{tot} = 2.68 \cdot 10^8$ M$_\odot$. Blue: Rescaled numerical solution with a total mass of $M_{tot}/10$.

1.7.2 Solitonic oscillations

A known feature of the solitonic solution are so-called solitonic oscillations. They arise from small perturbations to the soliton solution and cause the value of the central density of the soliton to oscillate. This property is well known and has been mentioned in sources such as [12], where the following formula for the frequency of these oscillations is given:

$$f = 10.94 \cdot \left(\frac{\rho_c}{10^{18}\ \mathrm{M}_\odot\,\mathrm{Mpc}^{-3}} \right)^{1/2} \frac{1}{\mathrm{Gyr}} \tag{1.30}$$

ρ_c is here the central density value of the soliton. Based on this formula one can conclude that solitons with higher central density (which corresponds to smaller core radius) have higher oscillation frequencies.

1.8 Energies of the FDM field

During the course of a simulation the FDM field will interact with a point mass and they might exchange energy. In this section we give an overview of the different energy components of the FDM field and in a later section we provide more details how the equations given in this section are implemented numerically in AxioNyx.

Here we will be working with units such that $\hbar = m_b = 1$. The total energy E_{FDM} of the FDM field can be calculated as (we work with the Lagrangian (1.8)):

$$\begin{aligned} E_{\rm FDM} &= \int_V d^3x \left\{ \frac{\partial \mathcal{L}}{\partial \dot{\psi}} \dot{\psi} + \frac{\partial \mathcal{L}}{\partial \dot{\psi}^*} \dot{\psi}^* + \frac{\partial \mathcal{L}}{\partial \dot{\Phi}} \dot{\Phi} - \mathcal{L} \right\} \\ &= \int_V d^3x \left\{ \frac{|\nabla \Phi|^2}{8\pi G} + \Phi |\psi|^2 + \frac{1}{2} |\nabla \psi|^2 \right\} \\ &= \int_V d^3x \left\{ \frac{1}{8\pi G} \nabla(\Phi \nabla \Phi) - \frac{1}{8\pi G} \Phi \nabla^2 \Phi + \Phi |\psi|^2 + \frac{1}{2} |\nabla \psi|^2 \right\} \end{aligned} \tag{1.31}$$

The above equation after using the Poisson equation (1.10) as well as applying Stokes' Theorem becomes

$$E_{\rm FDM} = \int_V d^3x \left\{ \frac{1}{2} \Phi |\psi|^2 + \frac{1}{2} |\nabla \psi|^2 \right\}. \tag{1.32}$$

When working with the soliton solution it is useful to once again use the Madelung transformation given by (1.11). The first term of (1.32) corresponds to the potential energy V of the FDM field:

$$V = \frac{1}{2} \int_V d^3x \ \Phi |\psi|^2 = \frac{1}{2} \int_V d^3x \ \rho \Phi. \tag{1.33}$$

The second term can be decomposed into a "kinetic" term K and a "quantum" term Q:

$$Q + K = \frac{1}{2} \int_V d\vec{x} |\nabla \psi|^2 = \frac{1}{2} \int_V d\vec{x} \left(|\nabla \sqrt{\rho}|^2 + \rho (\nabla \theta)^2 \right) \tag{1.34}$$

$$K = \frac{1}{2} \int_V d\vec{x} \rho (\nabla \theta)^2 = \frac{1}{2} \int_V d^3x \ \rho v^2 \tag{1.35}$$

$$Q = \frac{1}{2} \int_V d^3x \ |\nabla \sqrt{\rho}|^2 \tag{1.36}$$

where we used:

$$|\nabla \psi|^2 = |\nabla \sqrt{\rho} e^{i\theta}|^2 = (\nabla \sqrt{\rho})^2 + \rho (\nabla \theta)^2. \tag{1.37}$$

To sum up $E_{\rm FDM} = V + K + Q$. Based on these relations, we see that by knowing ψ and Φ at every point in some region of space the energies can be calculated by integrating over this region. In a simulation that contains only the FDM field without a point mass the components V, K, Q might change with time but the total energy E_{FDM} should be conserved in this case and this property can be used to test a code that evolves the Schrödinger-Poisson system.

1.9 FDM halos

In the following section the structure of FDM halos will be discussed. In [5] the authors presented results of simulations which showed that FDM halos have a solitonic core and an outside density profile that can be well fitted by the so-called "Navarro–Frenk–White" (NFW) profile. This NFW profile is the spherically-averaged density profile of halos formed by CDM, which have central cusps. This is in agreement with the statement that FDM does approach the behavior of CDM at large scales. Therefore in our simulations we will construct FDM halos having the same density profile as halos in CDM models (i.e. NFW profile) far from its center and a central soliton at its core as shown in Figure

1.4.
The NFW part of the halo which surrounds the central soliton is made up of excited states which can interfere with the solitonic core. In [14] the authors found that in simulations the solitonic core undergoes a confined random walk at the base of the halo potential and this was also investigated in [15] where the authors found that this random walk arises from interference between the ground state (the soliton) and the excited states that make up the halo surrounding the soliton.

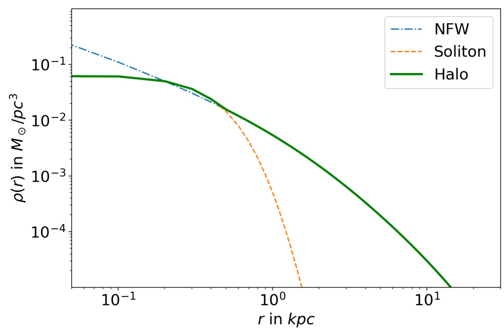

Figure 1.4: FDM halos have a density profile that has a soliton core and follows the NFW profile outside the core.

In [16] an important relationship between the virial halo mass M_{vir} and the soliton core radius r_c was found (for $a = 1$):

$$r_c = 1.6 \cdot \left(\frac{m_b}{10^{-22}\ \mathrm{eV}}\right)^{-1} \left(\frac{M_{\mathrm{vir}}}{10^9\ \mathrm{M}_\odot}\right)^{-1/3} \mathrm{kpc}. \tag{1.38}$$

As a consequence of this relation heavier halos have more concentrated solitonic cores. The numerical construction of FDM halos is discussed in section 3.3. In the next sections some more details regarding the NFW profile are given.

1.9.1 NFW density profile

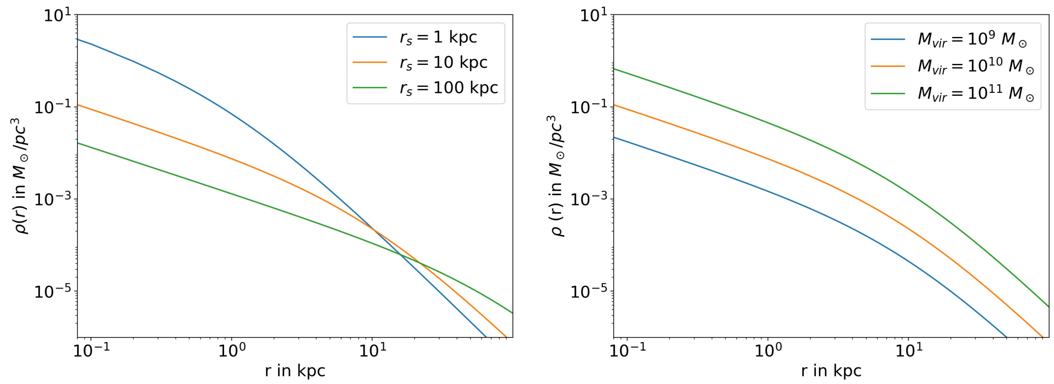

Figure 1.5: Left: NFW density profile for 3 different values of the scale radius r_s and a fixed virial mass $M_{\mathrm{vir}} = 10^{10} M_\odot$. Right: NFW density profile for 3 different values of the virial mass M_{vir} and a fixed scale radius $r_s = 10$ kpc.

The formula for the NFW density distribution [17], [18] is:

$$\rho_{\mathrm{NFW}}(r) = \frac{\rho_0}{\frac{r}{r_s}(1+\frac{r}{r_s})^2} \tag{1.39}$$

Just as in the solitonic profile the NFW profile also has two free parameters: the scale density ρ_0 and the scale radius r_s. When integrated up to infinity the total mass does not converge, but usually one considers this density profile only up to the virial radius r_{vir}. In practice, it is customary to take the virial radius r_{vir} as the radius at which the average inside a sphere with radius r_{vir} density is 200 times the critical density $\rho_{\mathrm{crit}} = \frac{3H^2}{8\pi G}$. The mass within this radius, also called the virial mass M_{vir}, is then

$$M_{\mathrm{vir}} = \frac{4}{3}\pi r_{\mathrm{vir}}^3 200 \cdot \rho_{\mathrm{crit}}. \tag{1.40}$$

This equation is also useful when one wants to find the virial radius r_{vir} for a given M_{vir}. Integrating the profile up to a radius R gives:

$$\begin{aligned} M(R) &= \int_0^R 4\pi r^2 \frac{\rho_0}{r/r_s(1+r/r_s)^2} dr = 4\pi\rho_0 r_s^3 \int_0^{R/r_s} \frac{r'}{(1+r')^2} dr' \\ &= 4\pi\rho_0 r_s^3 \int_0^{1+R/r_s} \frac{\tilde{r}-1}{\tilde{r}^2} d\tilde{r} = 4\pi\rho_0 r_s^3 \left[\log\left(\frac{r_s+R}{r_s}\right) + \frac{r_s}{r_s+R} - 1\right] \end{aligned}$$

Furthermore, when using the "concentration parameter" $c := r_{\mathrm{vir}}/r_s$ we can rewrite the virial mass M_{vir}, i.e. the mass within the virial radius r_{vir}, as:

$$M_{\mathrm{vir}} = M(r_{\mathrm{vir}}) = 4\pi\rho_0 r_s^3 \left[\log(1+c) - \frac{c}{1+c}\right] \tag{1.41}$$

Note that if r_s and M_{vir} are given, the equation can be inverted to calculate ρ_0, since c is also given from M_{vir} and r_s by using equation (1.40) to find r_{vir}.

The NFW density distribution falls off relatively slowly and has a "cusp" rather than a core at its center. Because the density does not fall of fast enough the total mass when integrating up to infinity does not converge. In simulations it is common to multiply the NFW profile with an exponential decay factor, in order to keep the total mass finite. To get a sense for how the parameters r_s and M_{vir} change the distribution see the Figure 1.5.

1.10 Possible mass of an FDM particle

Here we present some of the constraints on the mass m_b of the hypothetical FDM particle. Based on galactic dynamics, the authors of [19] tried to find a preferred mass range for m_b by studying dwarf spheroidal galaxies (dSph) with relatively old stellar populations. Concretely, they studied the problem of the longevity of a stellar clump in Ursa Minor, which has a stellar population age of $10-12$ Gyr and the mass m_b does have an effect on the dissolution timescale of the stellar clump. Furthermore they examined the problem of rapid orbital decay of the globular clusters in Fornax. Using N-body simulations they concluded that if all dark matter in the studied systems consisted of ultra-light scalar particles without self-interactions their mass would have to be in the range $3\cdot 10^{-23}$ eV $< m_b < 10^{-22}$ eV to explain the longevity of the stellar clump in Ursa Minor and the distribution of the globular clusters in Fornax.

Another paper that examined the possible mass range of ultra-light axionic dark matter is [20], focusing on constraints from the galaxy UV-luminosity function and reionization. The authors used an analytic model for the halo mass function of a DM model consisting either entirely of axions or a mixed model with half the DM consisting of axions and the other being CDM to determine the UV-luminosity function and then compared it to the UV-luminosity function from the Hubble Ultra Deep Field probe (e.g. see [21]) in the redshift range $z = 6 - 10$. They found that both models rule out $m_b \leq 10^{-23}$ eV, because in both scenarios not enough galaxies of the required magnitude at high z are produced to be consistent with the Hubble Ultra Deep Field probe, but taking $m_b = 10^{-22}$ eV does produce enough galaxies to be consistent with the probe. Furthermore, they found that in the model for reionization, taking $m_b = 10^{-23}$ eV does not reionize the universe by $z = 6$ and is inconsistent with the measured value of the optical depth to reionization τ, as measured from cosmic microwave background polarization. Importantly, $m_b = 10^{-22}$ eV is also at tension of 3σ with τ if all the dark matter consists of axions, but in the 50-50 mixed dark matter model this tension is reduced to 2σ. The paper concludes that $m_b = 10^{-22}$ eV is consistent with both the UV-luminosity function and the reionization of the universe in a wide range of models and was at the time of publication (2015) indistinguishable from CDM based on the mentioned observations. Further measurements of the UV-luminosity function in the range $z = 10 - 13$ by the James Webb space telescope, which makes observations in the infrared range required to observe redshifted UV light in the range $z = 10 - 13$, will provide evidence for or against $m_b = 10^{-22}$ eV.

The more recent paper [22], which was published relatively close (2022) to the writing of this work, examined the effect of FDM on cosmic shear, which is the distortion of images of distant galaxies due to weak gravitational lensing by the large-scale structure in the universe and it depends on the matter power spectrum, which is suppressed in FDM models compared to CDM. By using data from the Dark Energy Survey year 1 and observations of the cosmic microwave background anisotropies from the Planck space telescope the authors looked for shear correlation suppression caused by FDM and concluded that there is no evidence of suppression compared to the CDM model, but found another independent lower limit on the FDM particle mass m_b of 10^{-23} eV based on the results.

Another meaningful constraint comes from [23], where the authors used observations of the Lyman-alpha forest. The Lyman-alpha forest is a series of absorption lines in the spectra of distant galaxies caused by the Lyman-alpha electron transition of neutral hydrogen which is present in hydrogen clouds within the intergalactic medium. A bound for m_b can be extracted from the Lyman-alpha forest once again because FDM suppresses cosmological structure below a certain scale (the "Jeans scale", for more details see e.g. [12], [7]) and the Lyman-alpha forest can be used to get the matter power spectrum. In the paper the authors concluded that m_b has a lower bound of $2 \cdot 10^{-20}$ eV at 95% confidence.

Finally we will mention another recent paper [24] published in 2022, where the authors compared observations of ultra-faint dwarf galaxies with predictions for dynamical heating of stellar orbits from simulations of FDM halos and concluded that with 99% confidence m_b is greater than $3 \cdot 10^{-19}$ eV.

To conclude, the predictions made by FDM with $m_b \approx 10^{-21}$ eV are testable and in many cases the observational data ruled out models of FDM with m_b below a lower limit to be the only component of dark matter and it may be ruled out that FDM account for all of the dark matter. However, when considering that FDM accounts for only a fraction of dark matter the constraints are not that strong.

2 Relaxation

2.1 Relaxation time

When a star orbits in a galaxy, its trajectory will gradually change due to the effects of surrounding stars in the galaxy. This phenomenon is referred to as relaxation in the context of galactic dynamics. The relaxation time t_{relax} is defined as the time after which the cumulative "kicks" from many encounters with passing stars have perturbed the subject star's orbit significantly [25]. Importantly, after the relaxation time passes a star loses all its memory of its initial conditions [25]. It can be calculated in the following way:

$$t_{\text{relax}} = n_{\text{relax}} \cdot t_{\text{cross}}. \tag{2.1}$$

Here n_{relax} is the number of galaxy crossings required for the velocity of a star to change by an order of itself and t_{cross} is the time it takes for a single galaxy crossing, usually calculated as $t_{\text{cross}} = R/\sigma$ with R being the galaxy radius and v the velocity of the star. For a galaxy containing N stars r_{relax} may be estimated as (for more details see Chapter 7 in [25])

$$t_{\text{relax}} \approx 0.1 \frac{N}{\log N} t_{\text{cross}}. \tag{2.2}$$

Similarly, when a star or a test mass orbits through a medium of N particles with mass m, it will experience relaxation. In order to estimate the relaxation time t_{relax} one can plug into (2.2) the typical velocity $v = (GmN/R)^{1/2}$ (this velocity can be derived using the virial theorem, for more details see again Chapter 7 of [25]) to get [10]:

$$t_{\text{relax}} \sim \frac{v^3 R^3}{G^2 m^2 N \log N}. \tag{2.3}$$

In [10] the authors use this formula to point out that in plausible CDM models the particle mass m is usually so small that the resulting t_{relax} is much greater than the age of the universe and hence CDM halos are collisionless. However, a FDM model gives rise to density fluctuations which can be treated as quasiparticles with an effective mass m_{eff} that is large enough to make relaxation processes relevant.

2.2 Dynamical Friction in FDM

The phenomenon of dynamical friction in astrophysics was first discussed by Chandrasekhar in [26], where he has shown that a star will suffer from a systematic tendency to be decelerated in the direction of its motion as a consequence of the fluctuating force acting on a star due to the influence of its surrounding. Furthermore, Chandrasekhar concluded that the coefficient of dynamical friction must be of the order of the reciprocal relaxation time of the system.

Similarly, a test mass moving through FDM will exchange energy and momentum with the field and experience a drag force. This is due to the fact that its gravitational field will create an overdense region in the"wake" behind itself. In turn, the overdense region will "pull" on the particle and cause it to decelerate [11].

A detailed derivation and discussion of this effect can be found in [10] and [9]. The important steps and results will be briefly outlined in the following.

Assume that a test object with mass m_t moves through the FDM field and use a frame in which the test object is at rest at the origin and the FDM field with constant density ρ flows past with a velocity $\mathbf{v} = v_{rel}\hat{z}$. To simplify the problem only the gravitational interaction of the field with the particle will be considered and its self-gravity is ignored. In this case the wavefunction has to solve the time-independent Schrödinger equation $\hat{H}\psi = E\psi$, which in this case may be written as [11]:

$$\left[\frac{\hbar^2}{2m}\nabla^2 + \frac{Gm_tm_b}{r} + \frac{mv_{rel}^2}{2}\right]\psi = 0 \tag{2.4}$$

This problem is equivalent to the Coulomb scattering problem, where the solution to the time-independent Schrödinger equation is (e.g. see [27], with $e^2 \to G$, $Z_1 \to m_t$, $Z_2 \to m_b$ and $\xi \to \beta$):

$$\psi = Ne^{ikz}M(i\beta, 1, ik(r-z)) \tag{2.5}$$

Here $M(a, b, z)$ is a confluent hypergeometric function, $k = m_bv_{rel}/\hbar$ is the particle momentum, $\lambda_{dB} = h/m_bv_{rel}$ is the de Broglie wavelength and the parameter β is:

$$\beta = \frac{Gm_b^2m_t}{k\hbar^2} = 2\pi\frac{Gm_t}{v_{rel}^2\lambda_{dB}} = \frac{Gm_tm_b}{v_{rel}\hbar}. \tag{2.6}$$

The frictional force $\mathbf{F}_{\mathrm{DF}} = -F_{\mathrm{DF}}\hat{z}$ (here the DF stands for dynamical friction) acts on the particle in the opposite direction of its motion and the magnitude of this force is given by [9]:

$$F_{\mathrm{DF}} = \frac{4\pi G^2m_t^2\rho}{v_{rel}^2}C(\beta, kr) \tag{2.7}$$

Note that the r in the friction coefficient is supposed to be a cutoff radius around the test object up to which the contribution of the field is considered. For objects on circular orbits, it is appropriate to take the radius of the objects orbit [9]. In [9] the following expression for the friction coefficient C was found:

$$C(\beta, kr) = Cin(2kr) + \frac{\sin(2kr)}{2kr} - 1 + \mathcal{O}(\beta). \tag{2.8}$$

With $Cin(x) := \int_0^x (1-\cos(y))dy/y$. For the region close around the center of an FDM halo the limit $kr \ll 1$ is appropriate and C behaves as

$$C(kr) \approx \frac{1}{3}(kr)^2 \tag{2.9}$$

For a more detailed justification of this approximation see Appendix A . Meanwhile in the limit $kr \gg 1$ it can be shown [9] that C behaves as

$$C(\beta, kr) = \log(2kr) - 1 - \Re\mathfrak{e}\ \Psi(1+i\beta) + \mathcal{O}(1/kr) \tag{2.10}$$

with $\Psi(1 + i\beta)$ the digamma function, which for large β goes as $\log(\beta)$ and $-\gamma_E$ for small β (γ_E is the so-called Euler-Mascheroni constant). Through the effect of dynamical friction a test object in circular orbit around a solitonic core will begin to inspiral towards the center. In the following a rough estimate for the orbital decay timescale is provided. The velocity of a mass on a circular orbit is $v_c = (G\mathcal{M}(r)/r)^{1/2}$ (here $\mathcal{M}(r)$ denotes the mass contained within the radius r) and we use this velocity as the relative velocity v_{rel}

between the FDM field and the test object for our estimate. This gives for C:

$$C \approx \frac{1}{3}(kr)^2 = \frac{1}{3}\left(\frac{m_b v_{rel} r}{\hbar}\right)^2 = \frac{1}{3}\left(\frac{m_b}{\hbar}\right)^2 G r \mathcal{M}(r) \tag{2.11}$$

The friction force acting on a test mass on a circular orbit creates a torque $\boldsymbol{\tau}$ on the test mass. This torque will act opposite to the angular momentum L of the test mass causing it to lose angular momentum. The magnitude of the torque $\tau = r|F_{\mathrm{DF}}|$ is equal to the rate of change of the angular momentum and thus one can get a rough timescale $\mathcal{T}$ for the orbital decay of a test object with angular momentum $L = m_t r v_c$:

$$\mathcal{T} \approx \frac{|L|}{\tau} = \frac{|L|}{r|F_{\mathrm{DF}}|} = \frac{\mathcal{M}(r)^{3/2}}{4\pi G^{1/2} m_t \rho r^{3/2} C} \tag{2.12}$$

Using (2.11) one gets:

$$\mathcal{T} \sim \frac{3\mathcal{M}(r)^{1/2}\hbar^2}{4\pi G^{3/2} m_t m_b^2 \rho r^{5/2}} \tag{2.13}$$

In Figure 2.1 the red line shows the values of $\mathcal{T}$ for a particle with test mass $m_t = 10^6 M_\odot$ orbiting around a soliton with core mass $M_c = 2.8 \cdot 10^6 M_\odot$.

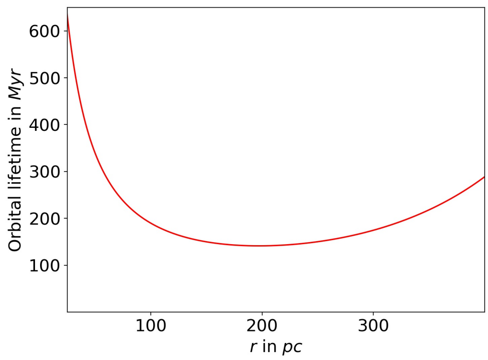

Figure 2.1: $\mathcal{T}$ as given by (2.13) for parameters as described above.

One can also use a similar argument to estimate the radial distance from the center of mass (we will refer to it as the (orbital) radius) as the test mass is decaying. Starting from

$$\frac{dL}{dt} = -|F_{\mathrm{DF}}| r \tag{2.14}$$

one can insert $L = m_t v_c r$ and (2.7) for F_{DF} and after rearranging the terms one arrives at

$$\frac{dr}{dt} = -\frac{4\pi G^2 m_t \rho r}{v_{rel}^2 v_c} C. \tag{2.15}$$

Next we will use the isothermal sphere formula for the density ρ as an approximation:

$$\rho = \frac{\sigma^2}{2\pi G r^2} = \frac{v_c^2}{4\pi G r^2}. \tag{2.16}$$

Finally, we will approximate the relative velocity v_{rel} between the FDM field and the test object with v_c, the velocity of the test object on a circular orbit. Plugging all that into the equation (2.15) gives

$$r\frac{dr}{dt} = -\frac{Gm_tC}{v_c}. \tag{2.17}$$

Also note that we are treating both C and v_c as constant with time. Separating the variables and integrating in time from $t = 0$ to $t = T$, in r from $r(0)$ to $r(T)$ respectively and solving for $r(T)$ leads to the equation

$$r(T) = \sqrt{r^2(0) - \frac{2Gm_tC}{v_c}T}. \tag{2.18}$$

Based on this formula due to dynamical friction the radius of a test object on a circular orbit through FDM will decrease over time and faster for more massive objects. However based on the simplifications used this formula is not expected to hold over longer time periods especially when the test object comes close to the halo/soliton center.

2.2.1 Fornax dwarf spheroidal galaxy

In this section we will discuss an actual example of a galaxy which provides observations that are not explainable by CDM but are consistent with the predictions of dynamical friction FDM discussed in the previous section, namely the Fornax dwarf spheroidal galaxy, which is a satellite galaxy of the Milky Way [9]. This galaxy contains 5 globular clusters that orbit at a length scale of about 1 kpc from the center of the Fornax dwarf spheroidal. If the globular clusters were moving through a cuspy CDM halo, they would sink towards the center of the galaxy in a few Gyr from their current position and therefore would not have survived until the present. This was presented in the paper [28] published in 2006, where the authors concluded that the Fornax dwarf spheroidal has a shallow inner density profile with a core.

In the Table I of [9] the orbital decay times for the globular clusters in Fornax are estimated assuming a FDM particle mass $m_b = 3 \cdot 10^{-22}$ eV and using the equation (2.12). The results show that 4 of the 5 clusters would have lifetimes of more than 10 Gyr and thus FDM provides a possible explanation for the existence of these globular clusters at the present time.

2.3 Relaxation in an FDM halo

The paper [10] provides a theoretical treatment of relaxation in FDM halos and in the following we discuss its most important results. Note however, that most of the results are based on numerous simplifying assumptions.

First lets introduce the Coulomb logarithm $\Lambda = b_{\text{max}}/b_{\text{min}}$, a common quantity used when studying relaxation in galactic systems (e.g. see [25]), defined as the ratio between the maximal b_{max} and minimal b_{min} length scales of encounters which are relevant for relaxation. In classical systems one takes $b_{\text{min}} = b_{90} = (Gm/\sigma^2)$ to be the typical distance at which a test mass would be deflected by 90°. In the discussed paper, the authors show that it is appropriate to take $b_{\text{min}} = \lambda\!\!\!^{-}_\sigma/2 = \hbar/2m_b\sigma$ for FDM quasiparticles, so they define the Coulomb logarithm for FDM quasiparticles Λ_{FDM} as

$$\Lambda_{\text{FDM}} = \frac{b_{\text{max}}}{\lambda\!\!\!^{-}/2} = \frac{2b_{\text{max}}m_b\sigma}{\hbar} \tag{2.19}$$

while for comparison the classical Coulomb logarithms Λ_{cl} reads

$$\Lambda_{cl} = \frac{b_{\max}}{b_{90}} = \frac{b_{\max}\sigma^2}{Gm}. \tag{2.20}$$

Note that the precise values of the Coulomb logarithm are uncertain by a factor of order unity [10].
Next it is important to mention that the authors of the paper expand the wavefunction of the FDM field into a collection of plane waves and denote the velocity distribution function (DF) of these waves as $F_b(\vec{v})$. This DF is important because the authors used it to derive the effective velocity DF of the quasiparticles

$$F_{\text{eff}}(\vec{v}) = \frac{\int d\vec{v} F_b(\vec{v})}{\int d\vec{v} F_b^2(\vec{v})} F_b^2(\vec{v}) \tag{2.21}$$

and the effective mass m_{eff} of the quasiparticles

$$m_{\text{eff}} = \frac{(2\pi\hbar)^3 \int d\vec{v} F_b^2(\vec{v})}{m_b^3 \int d\vec{v} F_b(\vec{v})}. \tag{2.22}$$

When using the simplifying assumption that the velocity DF is Maxwellian, which is justified by the results of previous simulations presented in [29], we get for $F_b(\vec{v})$

$$F_b(\vec{v}) = \frac{\rho}{(2\pi\sigma^2)^{3/2}} e^{-v^2/(2\sigma^2)}. \tag{2.23}$$

Then m_{eff} evaluates to

$$m_{\text{eff}} = \frac{\pi^{3/2}\hbar^3\rho}{m_b^3\sigma^3} = \rho(f\lambda_\sigma)^3 \tag{2.24}$$

with $f = 1/(2\pi^{1/2}) \approx 0.282$. To estimate the value of m_{eff} in (2.24) the authors of the discussed paper used the common approximation that the density ρ is related to σ by the formula used for an isothermal sphere (2.16) and get in this case

$$m_{\text{eff}} = \frac{\pi^{1/2}\hbar^3}{2^{1/2}Gm_b^3 v r^2} = 1.03 \cdot 10^7 \text{ M}_\odot \left(\frac{r}{1 \text{ kpc}}\right)^{-2} \left(\frac{m_b}{10^{-22} \text{ eV}}\right)^{-3} \left(\frac{v_c}{200 \text{km s}^{-1}}\right)^{-1}. \tag{2.25}$$

The effects of the encounters with the FDM field on a point mass ("test object") can be described by 3 independent diffusion coefficients [25]: $D[\Delta v_\parallel]$, $D[(\Delta v_\parallel)^2]$ and $D[(\Delta v_\perp)^2]$ when using coordinates such that $v_\parallel$ is the velocity of the point mass. The first-order coefficient describes the expectation of change in $v_\parallel$ per unit time and corresponds to a steady drift through phase space. The second-order coefficients corresponds to the rate at which the point mass performs a random walk through phase space. The rate of change in the specific energy of the point mass is given by $D[\Delta E]$ and be calculated from the 3 independent coefficients as:

$$D[\Delta E] = vD[\Delta v_\parallel] + \frac{1}{2}D[(\Delta v_\parallel)^2] + \frac{1}{2}D[(\Delta v_\perp)^2]. \tag{2.26}$$

For more details on diffusion coefficients in astrophysical context see section 7.4.4 in [25].

In the paper [10] the authors considered two independent contributions to the diffusion coefficients, one from the effect of dynamical friction, which was already introduced in more details in the previous section and another effect from the stochastic density fluctuations ("granules") of the FDM field. The authors derived the following for the $D[\Delta v_\parallel]$ diffusion coefficients for both effects:

$$\begin{aligned} D_S[\Delta v_\parallel] &= -\frac{4\pi G^2 \rho m_{\mathrm{eff}} \log \Lambda_{\mathrm{FDM}}}{\sigma_{\mathrm{eff}}^2} G(X_{\mathrm{eff}}) \\ D_{\mathrm{DF}}[\Delta v_\parallel] &= -\frac{2\pi G^2 \rho m_t \log \Lambda_{\mathrm{FDM}}}{\sigma_{\mathrm{eff}}^2} G(X) \end{aligned} \tag{2.27}$$

They defined the important ratio

$$\mu_{\mathrm{eff}} = m_t/2m_{\mathrm{eff}} \tag{2.28}$$

and with that the diffusion coefficient $D[\Delta v_\parallel]$ is

$$\begin{aligned} D[\Delta v_\parallel] &= D_S[\Delta v_\parallel] + D_{\mathrm{DF}}[\Delta v_\parallel] \\ &= -\frac{4\pi G^2 \rho m_{\mathrm{eff}} \log \Lambda_{\mathrm{FDM}}}{\sigma_{\mathrm{eff}}^2} \Big[G(X_{\mathrm{eff}}) + \mu_{\mathrm{eff}} G(X) \Big] \end{aligned} \tag{2.29}$$

with $\sigma_{\mathrm{eff}} = \sigma/\sqrt{2}$, $X = v/\sqrt{2}\sigma$, $X_{\mathrm{eff}} = v/\sqrt{2}\sigma_{\mathrm{eff}}$, and

$$\begin{aligned} G(X) &= \frac{1}{2X^2}\left[\mathrm{erf}\,(X) - X\frac{d}{dX}\,\mathrm{erf}\,(X) \right] \\ &= \frac{1}{2X^2}\left[\mathrm{erf}\,(X) - \frac{2X}{\sqrt{\pi}} e^{-X^2} \right]. \end{aligned} \tag{2.30}$$

Here erf (x) is the (Gauss) error function. The result in equation (2.29) is the sum of the two terms $D_S[\Delta v_\parallel]$ and $D_{\mathrm{DF}}[\Delta v_\parallel]$. The first one being the contribution from stochastic density fluctuations in the FDM halo which leads to diffusion of the velocity of a zero-mass test object and does not contain m_t, the mass of the test object orbiting in the FDM halo. The second term is the contribution of dynamical friction, a phenomenon discussed in more detail in section 2.2.

Meanwhile, for $D[(\Delta v_\parallel)^2]$ and $D[(\Delta v_\perp)^2]$ they shown:

$$\begin{aligned} D[(\Delta v_\parallel)^2] &= \frac{4\sqrt{2}\pi G^2 \rho m_{\mathrm{eff}} \log \Lambda_{FDM}}{\sigma_{\mathrm{eff}}} \frac{G(X_{\mathrm{eff}})}{X_{\mathrm{eff}}} \\ D[(\Delta v_\perp)^2] &= \frac{4\sqrt{2}\pi G^2 \rho m_{\mathrm{eff}} \log \Lambda_{FDM}}{\sigma_{\mathrm{eff}}} \frac{\mathrm{erf}\,(X_{\mathrm{eff}}) - G(X_{\mathrm{eff}})}{X_{\mathrm{eff}}} \end{aligned} \tag{2.31}$$

For these two coefficients only the stochastic density fluctuations contribute and thus they do not depend on the test object mass m_t. In the paper [10] the authors also calculated the specific energy diffusion coefficient $D[\Delta E]$

$$D[\Delta E] = \frac{8\sqrt{\pi} G^2 \rho m_{\mathrm{eff}} \log \Lambda_{FDM}}{\sigma} \exp\,(-v^2/\sigma^2)[1 - \mu_{\mathrm{eff}} K(v/\sigma)] \tag{2.32}$$

with

$$K(x) := \frac{\sqrt{\pi}}{x} e^{x^2}\,\mathrm{erf}\,(x/\sqrt{2}) - \sqrt{2} e^{x^2/2}.$$

Based on this result the authors concluded the following: the mean change in energy of a test object with mass m_t orbiting in an FDM halo consists of two opposite contributions called "heating" (diffusion) and "cooling" (dynamical friction). The heating results from the density fluctuations of the FDM field is proportional to m_{eff}, while the cooling is the dynamical friction resulting from the wake that forms behind a massive object and it is proportional to m_t. These effects are opposite in the sense that the heating transfers energy from the FDM field to the test object and the cooling vice versa [10].

Since these effects are proportional to m_t and m_{eff}, one can determine by the ratio μ_{eff} which one will dominate, i.e. when $\mu_{\text{eff}} \ll 1$ (i.e. $m_t \ll m_{\text{eff}}$) the heating dominates and the test object will gain energy. Meanwhile when $\mu_{\text{eff}} \gg 1$ (i.e. $m_t \gg m_{\text{eff}}$) cooling will be the dominating effect and the test object should lose energy.

Based on the results the authors of [10] concluded that a massive object orbiting in an FDM halo will inspiral towards the central soliton if $\mu_{\text{eff}} \gg 1$. The inspiral time t_{in} can be calculated from the usual formula (eq. 8.12) given in [25] using Λ_{FDM} and it evaluates to [10]:

$$t_{in} = \frac{1.65 r_i^2 \sigma}{\log \Lambda_{\text{FDM}} G m_t} = \frac{84.9\ \text{Gyr}}{\log \Lambda_{\text{FDM}}} \frac{10^7 M_\odot}{m_t} \frac{v_c}{200\ \text{km s}^{-1}} \left(\frac{r_i}{4\ \text{kpc}} \right)^2 . \tag{2.33}$$

However, when the object radius r shrinks, the effective mass of the FDM quasiparticles m_{eff} grows like r^{-2} (from equation (2.25) which uses the isothermal sphere approximation), which means that the mass ratio μ_{eff} is proportional to r^2. Then μ_{eff} will ultimately become less than 1 inside the so-called stalling radius r_{stall} given as [10]

$$\begin{aligned} r_{\text{stall}} &= (2\pi)^{1/4} \left(\frac{\hbar^3}{G m_t m_b^3 v_c} \right)^{1/2} \\ &= 1.43\ \text{kpc} \left(\frac{m_t}{10^7 \text{M}_\odot} \right)^{-1/2} \left(\frac{m_b}{10^{-22}\ \text{eV}} \right)^{-3/2} \left(\frac{v_c}{200\ \text{km s}^{-1}} \right)^{-1/2} . \end{aligned} \tag{2.34}$$

This result suggests that the inspiral of massive objects may be stalled in FDM halos.

3 Numerical methods

3.1 AxioNyx

For simulations in this work we use AxioNyx [29], an extended version of the Nyx code [30], which supports block structured adaptive mesh refinement (AMR) and can run in parallel on multiple cores of a cluster. AxioNyx features a Schrödinger-Poisson solver that works on adaptively refined meshes and was developed to facilitate detailed explorations of astrophysical consequences of FDM. In the following sections some relevant details regarding AxioNyx are outlined.

3.1.1 Dynamical evolution of the FDM field

The dynamical evolution on the root grid is done according to the time dependent Schrödinger equation (1.9) via a split-step Fourier method (also called pseudospectral method) on a $N \times N \times N$ grid with periodic boundary conditions, as described in e.g. [13]. In the following this method is briefly explained. For simplicity, let us work with units such that $\hbar = 1$, $G = 1$ and $m_b = 1$. Starting from the Schrödinger equation:

$$i\dot{\psi} = H\psi(t, \vec{x}) \tag{3.1}$$

with the Hamiltonian H, which consists of a kinetic part and a gravitational potential part:

$$H = -\frac{1}{2}\nabla^2 + \Phi \tag{3.2}$$

The time evolution operator $U(t, t_0)$ is in general given as:

$$U(t, t_0) = \exp\left[-i \int_{t_0}^{t} dt' H(t') \right] \tag{3.3}$$

where t_0 is the initial time and t is some later time. Applied to our specific case with the Hamiltonian (3.2) and taking $t = t_0 + dt$ one arrives at

$$U(t_0 + dt, t_0) = \exp\left[-i \int_{t_0}^{t_0+dt} dt' \bigg(-\frac{1}{2}\nabla^2 + \Phi(t', \vec{x}) \bigg) \right]. \tag{3.4}$$

Next we will assume that t and t_0 are separated by only a small time difference, i.e. dt is small such that the integral may be approximated with the trapezoidal rule given in (3.5) as follows:

$$\int_{b}^{a} f(x)dx \approx \frac{(b-a)}{2}(f(a) + f(b)) \tag{3.5}$$

$$\int_{t_0}^{t_0+dt} dt' \bigg(-\frac{1}{2}\nabla^2 + \Phi(t', \vec{x}) \bigg) \approx \frac{dt}{2} \bigg(-\nabla^2 + \Phi(t_0 + dt, \vec{x}) + \Phi(t_0, \vec{x}) \bigg). \tag{3.6}$$

Therefore for small timesteps dt we get

$$\begin{aligned} \psi(t_0 + dt, \vec{x}) &= U(t_0 + dt, t_0)\ \psi(t_0, \vec{x}) \\ &= \exp\left[i\frac{dt}{2} \bigg(\nabla^2 - \Phi(t_0 + dt, \vec{x}) - \Phi(t_0, \vec{x}) \bigg) \right] \psi(t_0, \vec{x}). \end{aligned} \tag{3.7}$$

For small timesteps this can be rewritten as [13]

$$\psi(t_0+dt,\vec{x}) \approx \exp\left[-\frac{idt}{2}\Phi(t_0+dt,\vec{x})\right]\exp\left[-\frac{idt}{2}\nabla^2\right]\exp\left[-\frac{idt}{2}\Phi(t_0,\vec{x})\right]\psi(t_0,\vec{x}). \tag{3.8}$$

A justification for this step for small timesteps can be obtained from the Baker-Campbell-Hausdorff formula stating: Given the operators X and Y, the product of their exponentials is

$$\begin{aligned} e^X e^Y &= e^{Z(X,Y)} \\ \text{with} \qquad Z(X,Y) &= X+Y+\frac{1}{2}[X,Y]+\frac{1}{12}[X,[X,Y]]-\frac{1}{12}[Y,[X,Y]]+... \end{aligned} \tag{3.9}$$

Here $[X,Y] := XY - YX$ denotes the commutator. First, we apply this formula to (3.8) with $X = \frac{idt}{2}\nabla^2$ and $Y = -\frac{idt}{2}\Phi(t_0,\vec{x})$ which gives for $Z(X,Y)$ up to order dt^2:

$$Z(X,Y) = \frac{idt}{2}\Big(\nabla^2 - \Phi(t_0,\vec{x})\Big) + \frac{dt^2}{8}[\nabla^2, \Phi(t_0,\vec{x})]. \tag{3.10}$$

Thus Z combined the last two exponential factors of Equation (3.8). The combination that includes all three factors will be denoted Z'.

Using the Baker-Campbell-Hausdorff formula again with $X = \frac{idt}{2}(\nabla^2 - \Phi(t_0,\vec{x})) + \frac{dt^2}{8}[\nabla^2, \Phi(t_0,\vec{x})]$ and $Y = -\frac{idt}{2}\Phi(t_0+dt,\vec{x})$ gives (we keep only terms up to order dt^2):

$$Z'(X,Y) = \frac{idt}{2}\Big(\nabla^2 - \Phi(t_0,\vec{x}) - \Phi(t_0+dt,\vec{x})\Big) + \frac{dt^2}{8}[\nabla^2, \Phi(t_0,\vec{x})]. \tag{3.11}$$

Thus we can rewrite the evolution operator in (3.7) as

$$\begin{aligned} \exp\Bigg[\frac{idt}{2}&\Big(\nabla^2 - \Phi(t_0+dt,\vec{x}) - \Phi(t_0,\vec{x})\Big) \\ &+\frac{dt^2}{8}\Big([\nabla^2, \Phi(t_0,\vec{x})] - [\nabla^2, \Phi(t_0+dt,\vec{x})]\Big)\Bigg]. \end{aligned} \tag{3.12}$$

When using $\Phi(t_0+dt,\vec{x}) \approx \Phi(t_0,\vec{x}) + dt\dot{\Phi}(t_0,\vec{x})$ in the second line of the above expression, we find that it will only contain terms of order dt^3. So up to dt^2 the expression simplifies to the evolution operator in (3.7), which is what we wanted to show.

Furthermore, by switching to the frequency domain, the derivatives become simple multiplications. Concretely, one performs a Fourier transform $\mathcal{F}$ after an initial half step based on the gravitational field $\Phi(t_0,\vec{x})$ is performed ("kick"). Then the multiplication gets applied ("drift") and after an inverse Fourier transform back into the original domain finally a second half step ("kick") is applied, this time using $\Phi(t_0+dt,\vec{x})$. This algorithm can be summarized by the formula

$$\begin{aligned} &\psi(t_0+dt,\vec{x}) = \\ &\exp\left[-\frac{idt}{2}\Phi(t_0+dt,\vec{x})\right]\mathcal{F}^{-1}\exp\left[-\frac{idt}{2}k^2\right]\mathcal{F}\exp\left[-\frac{idt}{2}\Phi(t_0,\vec{x})\right]\psi(t_0,\vec{x}). \end{aligned} \tag{3.13}$$

However, when implementing this numerically one needs to update the gravitational potential, e.g. calculate $\Phi(t_0+dt,\vec{x})$ by solving the Poisson equation. This can be done by applying a Fourier transform on (1.10), which again transforms the nabla operator into a multiplication and then solving for Φ gives:

$$\Phi = \mathcal{F}^{-1}\left[\left(-\frac{4\pi}{k^2}\right)\mathcal{F}(|\psi|^2)\right] \tag{3.14}$$

Since we want to use this result to get $\Phi(t_0+dt,\vec{x})$, we can plug in $\psi(t_0+dt/2,\vec{x})$, which is ψ at the half-step, i.e. after $\exp\left[-\frac{idt}{2}\Phi(t_0,\vec{x})\right]$ has been applied. With that we get

$$\Phi(t_0+dt,\vec{x}) = \mathcal{F}^{-1}\left[\left(-\frac{4\pi}{k^2}\right)\mathcal{F}(|\psi(t_0+dt/2,\vec{x})|^2)\right]. \tag{3.15}$$

Furthermore, before the inverse Fourier transform is performed the $k=0$ Fourier mode is set to zero. The method just described here is 2nd order accurate and in AxioNyx a more accurate 6th order scheme is also available, which we use in our simulations. For more details regarding the 6th order scheme see [29] (e.g. see equation (3) and TABLE I).

When using mesh refinement, the refined regions do not have periodic boundary conditions and therefore one cannot use the pseudospectral method in those regions. AxioNyx uses instead a fourth order Runge-Kutta solver to solve equation (1.9) on the refined sub grids. The ∇^2 is approximated using a 6th order finite differencing scheme which utilizes a stencil that uses all the adjacent cell values of a given cell i.e. consists of a cube with 3 by 3 by 3 cells. However, using finite differencing instead of the pseudospectral method is slower.

3.1.2 Energies in AxioNyx

Calculating the energy during a simulation is in our case important for two main reasons: Firstly, the total energy should be a conserved quantity during a simulation and if this is violated then something is going wrong with our simulation. Secondly, as part of our study of the dynamics of a test object orbiting in an FDM soliton/halo we need to keep track of the energy of both the FDM field and the test object, since the theory outlined in Chapter 3 (in section 2.3) predicts that there are scenarios in which the test object loses energy to the FDM field as well as scenarios where a test object may gain energy from the FDM field. As discussed in Chapter 2, the energy of the FDM field can be decomposed into 3 parts: 1. gravitational potential energy V; 2. kinetic part K; 3. "quantum" energy Q. V, K and Q are defined as in (1.33), (1.35) and (1.36). The sum of the two latter energies is denoted E_{kin}. In AxioNyx, these energies are computed as described below.

The derivatives in the K term is approximated using a 1st order finite difference scheme, while when calculating the sum of $K+Q$ from (1.34) and Q, a 2nd order finite difference method is used to calculate the derivatives. At this point it should be mentioned that in the source code, V, K, Q and $Q+K$ are called $E_{\text{pot}}, E_{\text{kinv}}$, E_{kinrho} and E_{kin} respectively.

3.1.3 Test object time evolution

The time evolution of a massive test object modelled as a point mass in the simulations is done using a modified version of the Nyx code, which employs a move-kick-drift algorithm for this purpose[2]. In the following we will briefly outline how the time evolution is performed in the code for a single point mass.

Let $\mathbf{x}$ be the location and $\mathbf{v}$ the velocity of the test mass, then we have to solve the following system of equations:

$$\begin{aligned} \frac{d\mathbf{x}}{dt} &= \frac{1}{a}\mathbf{v} \\ \frac{d(a\mathbf{v})}{dt} &= \mathbf{g}. \end{aligned} \tag{3.16}$$

Here $\mathbf{g} = \mathbf{g}(\mathbf{x}, t)$ is the gravitational acceleration evaluated at the location of the particle at time t and a is the scale factor. In our simulations we will take $a = 1$ to be constant so we will drop it in the following. To evolve the position $\mathbf{x}^n$ and velocity $\mathbf{v}^n$ from timestep n to $n+1$ ($t^{n+1} = t^n + \Delta t$) the following steps are performed (for more details see documentation given in the NYX documentation[2] or in [30]):

1. Calculate $\mathbf{g}^n$
2. $\mathbf{v}^{n+1/2} = \mathbf{v}^n + \frac{\Delta t}{2}\mathbf{g}^n$
3. $\mathbf{x}^{n+1} = \mathbf{x}^n + \Delta t\ \mathbf{v}^{n+1/2}$
4. Calculate for $\mathbf{g}^{\mathbf{n+1}}$ using $\mathbf{x}^{n+1}$
5. $\mathbf{v}^{n+1} = (\mathbf{v}^{n+1/2} + \frac{\Delta t}{2}\mathbf{g}^{n+1})$

Note that $\mathbf{g}$ is computed as $\mathbf{g} = -\nabla\Phi$. Since Φ is discretized, interpolation is used to calculate $\mathbf{g}$ at any position.

3.2 Initial conditions

3.2.1 Test mass on a circular orbit

To set the initial conditions of a test mass (a point mass) on a circular orbit with an initial distance r_i from the center of a soliton or FDM halo we will determine its initial velocity at this distance with the formula

$$v_c = \sqrt{\frac{GM(r_i)}{r_i}} = \left(4.3 \cdot 10^{-3} \frac{M(r_i)}{\mathrm{M}_\odot} \frac{\mathrm{pc}}{r_i}\right)^{1/2} \frac{\mathrm{km}}{\mathrm{s}} \tag{3.17}$$

where $M(r_i)$ is the mass of the FDM field in solar masses enclosed within the radius r_i (in pc) and may be calculated by integrating the density up to this radius

$$M(r_i) := 4\pi \int_0^{r_i} dr \rho(r) r^2. \tag{3.18}$$

[2]amrex-astro.github.io/Nyx/docs_html/Particles.html#equations

3.2.2 Initial soliton density

To get the initial soliton density for a simulation where the FDM field consists only of a soliton we use a slightly rewritten version of (1.28):

$$\rho_s(r) = \frac{\rho_0}{(1 + 0.091 \cdot \frac{r^2}{r_c^2})^8} \tag{3.19}$$

with the central density ρ_0

$$\rho_0 = 0.0194 \cdot \left(\frac{10^{-22}\ \mathrm{eV}}{m_b}\right)^2 \cdot \left(\frac{\mathrm{kpc}}{r_c}\right)^4 \frac{\mathrm{M}_\odot}{\mathrm{pc}^3}. \tag{3.20}$$

Next, when the wavefunction is written as $\psi = \sqrt{\rho} e^{i\theta}$ it can be split into a purely real $Re(\psi)$ and imaginary part $Im(\psi)$:

$$Re(\psi) = \sqrt{\rho} \cos\theta \tag{3.21}$$

$$Im(\psi) = \sqrt{\rho} \sin\theta. \tag{3.22}$$

The initial velocity of the soliton solution is then

$$\vec{v} = \frac{\hbar}{m} \vec{\nabla}\theta. \tag{3.23}$$

We want to set up a soliton initially at rest so θ has to be constant and the easiest way to achieve this is to set $\theta = 0$ initially. Then the imaginary part $Im = 0$ and the real part will be:

$$Re(\psi) = \left(\frac{\rho_0}{(1 + 0.091 \cdot \frac{r^2}{r_c^2})^8}\right)^{1/2}. \tag{3.24}$$

It is a bit inconvenient to use r_c as a parameter to set up the initial profile and we will instead use the soliton core mass M_c, which is related to the total soliton mass by the relation $M_s \sim 4M_c$. This can be achieved using a relation between the core radius r_c and the core mass M_c [31]:

$$r_c = 8.64 \cdot \frac{\mathrm{M}_\odot}{\mathrm{M_c}} \cdot \left(\frac{2.5 \cdot 10^{-22}\ \mathrm{eV}}{m_b}\right)^2 \mathrm{Mpc}. \tag{3.25}$$

With that we can specify the FDM particle mass m_b and soliton core mass M_c to set up the initial density profile using (3.25) and (3.24). Note that when performing simulations in an FDM halo we use instead the method described in 3.3.

3.3 Construction of FDM halos

To construct FDM halos we follow the method presented by T. Yavetz et al. (2021) in [32] (also see [33]), where they presented a way to construct self-consistent halos consisting of superpositions of eigenmodes chosen such as to produce a target mean density profile. The idea of the construction is to first compute a “library” of wave eigenmodes in the target gravitational potential and then to choose an appropriate superposition of the eigenmodes to reproduce the target density profile. In the following we show the details of this method. As usual the starting point is the Schrödinger-Poisson system of equations ((1.9) and (1.10)). Recall that the Schrödinger equation in our case is

$$i\hbar\dot{\psi} = \left(-\frac{\hbar^2}{2m_b}\nabla^2 + m_b\Phi \right)\psi. \tag{3.26}$$

We are constructing an FDM halo in local equilibrium with a static potential profile which means that the halo should have no long term evolution. Hence as a first order approximation we treat the gravitational potential Φ and the Hamiltonian H as time independent. Note however that the FDM halo still exhibits density fluctuations on short time scales.

We decompose the wavefunction $\psi(\vec{x}, t)$ as a sum of normalized orthogonal spatial eigenmodes $\psi_j(\vec{x})$, i.e.:

$$\psi(\vec{x}, t) = \sum_j a_j \psi_j(\vec{x}) e^{-iE_j t/\hbar}. \tag{3.27}$$

Here a_j is a complex amplitude associated with the eigenmode ψ_j. The eigenmodes ψ_j all satisfy the time independent Schrödinger equation $\hat{H}\psi = E\psi$, which in our case becomes

$$\left(-\frac{\hbar^2}{2m_b}\nabla^2 + m_b\Phi \right)\psi_j = E_j\psi_j \tag{3.28}$$

where E_j is the energy eigenvalue of the mode ψ_j and the expression for the number density will be

$$\begin{aligned} |\psi(\vec{x}, t)|^2 &= \left| \sum_j a_j \psi_j(\vec{x}) e^{-iE_j t/\hbar} \right|^2 \\ &= \left| \sum_j a_j \psi_j(\vec{x}) \right|^2 + \left| \sum_{j \neq k} a_j a_k^* \psi_j(\vec{x}) \psi_k^*(\vec{x}) e^{i(E_k - E_j)t/\hbar} \right|^2. \end{aligned} \tag{3.29}$$

The second term is time dependent and describes the interference between different eigenmodes. It is responsible for the FDM density fluctuations (also called "granules").

Under time averaging the density becomes:

$$\langle |\psi(\vec{x}, t)|^2 \rangle = \left| \sum_j a_j \psi_j(\vec{x}) \right|^2. \tag{3.30}$$

When constructing an FDM halo the goal is to find the coefficients a_j such that $\langle |\psi(\vec{x}, t)|^2 \rangle$ matches a target density profile.

We are interested in a target profile that corresponds to an FDM halo profile as described in Section 1.9. The inner profile has to follow a soliton density profile and the outer profile has to follow a NFW profile, which in order to keep the halo mass finite is multiplied with $\exp(-r/2r_{\text{vir}}^2)$. One example of such a halo is shown in Figure 1.4. In the next section the calculation of eigenmodes is discussed.

3.3.1 Calculating eigenmodes

Since our target halo is spherically symmetric, we use the Ansatz $\psi_{nlm}(r, \theta, \phi) = R_{nl}(r) Y_l^m(\theta, \phi)$ to find the eigenmodes. After substituting $u(r) := rR_{nl}(r)$ the Schrödinger equation becomes (for more details see e.g. section 2.1 in [27]):

$$-\frac{\hbar^2}{2m_b}\frac{d^2u}{dr^2}+\left[\frac{\hbar^2}{2m_b}\frac{l(l+1)}{r^2}+m_b\Phi(r)\right]u=E_{nl}u. \tag{3.31}$$

The energy E_{nl} depends only on n and l because of spherical symmetry. Next we compute the gravitational potential $\Phi(r)$ of the target density profile (FDM profile) by integrating the Poisson equation. This calculation is done numerically up to a maximum radius which we take to be ten times the virial radius.

When calculating the eigenmodes we will consider all values for n and l between 0 up to the cutoff value N_r, which will be the same as the number of grid points for the radius r which lie between 0 and $r_{\max}=r_{\rm vir}$. This means that we initially compute N_r^2 eigenmodes ψ_{nlm}. To reduce the number of eigenmodes for the construction of the FDM halo we will only keep eigenmodes with energy less than the potential energy E_m of a particle on a virial orbit ($E_m=-GM_{\rm vir}/2r_{\rm vir}$). The number of valid eigenmodes which we keep will be denoted as N_p.

3.3.2 Determination of amplitudes

Recall that the goal was to find the amplitudes a_j which produce the target density profile (FDM halo profile) when averaged over time. One can achieve this with the following steps:

1. Choose the target density distribution ρ_t.
2. Calculate gravitational potential corresponding to ρ_t.
3. Calculate eigenmodes of ρ_t.
4. Find a superposition of eigenmodes which produces the target density ρ_t (our target density is the FDM halo profile, $\rho_t=\rho_{\rm FDM}$), i.e. determine $|a_j|^2$.

Recall that a_j is complex, so it has a phase which has no impact on the time averaged density profile and can therefore be chosen randomly. Furthermore when constructing a spherically symmetric profile a_{nlm} is independent of m and we will be using the following relation:

$$\sum_m |Y_l^m(\theta,\phi)|^2=\frac{2l+1}{4\pi}. \tag{3.32}$$

$|a_{nlm}|^2$ will be determined by minimizing the “cost function”:

$$D(\rho_t,\rho_{out})=\frac{1}{r_{\rm fit}}\int_0^{r_{\rm fit}}dr\left(\frac{\rho_{out}-\rho_t}{\rho_t}\right)^2 \tag{3.33}$$

where ρ_t is the target density profile, $r_{\rm fit}$ is the maximum radius up to which the fit is being performed and ρ_{out} is given as:

$$\rho_{out}(r)=\langle|\psi(\vec{x},t)|^2\rangle=\sum_{nlm}|a_{nlm}R_{nl}(r)Y_l^m(\theta,\phi)|^2.$$

$$=\frac{1}{4\pi}\sum_{nl}|a_{nl}|^2|R_{nl}(r)|^2(2l+1). \tag{3.34}$$

We used one more additional constraint called the "isotropic fit" [32], where we use the energy E_{nl} to put together eigenmodes into bins based on their energy and require that all a_{nlm} are the same for eigenmodes within the same energy bin. When setting up our simulations we used 100 bins. To sum up, the required input parameters to construct an FDM halo are m_b, r_s, r_{vir} and N_r.

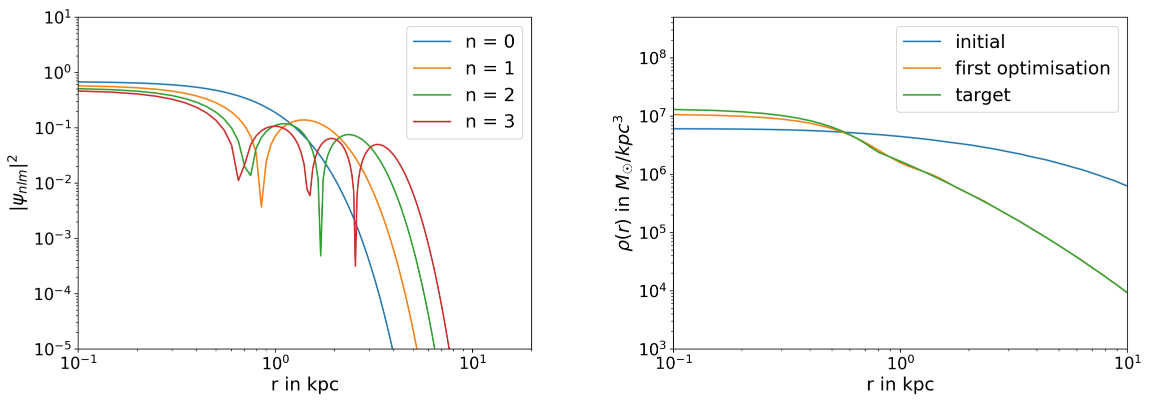

Figure 3.1: Left: First couple of eigenmodes ψ_{nlm} from a construction of an FDM halo. Right: The initial density corresponds to the density before the optimization with all the $a_{nlm} = 1$. After an optimization the result is close to the target density.

Note that the virial mass M_{vir} can be calculated when given r_{vir} with equation (1.40). One can determine ρ_0 for the NFW profile from equation (1.41). To get r_c of the core soliton we use the relation between the core radius and the halo mass given by (1.38). As an example of the construction process in the left panel of Figure 3.1 the first couple of eigenmodes are plotted from a construction of an FDM halo. In the right panel the initial guess for the density profile as well as the target density together with the result of the first optimization are shown. After an additional second optimization the resulting density profile matches the target density perfectly.

3.4 Computational cost

To give the reader some idea about the computational resources used for the simulations, we used typically 64 cpu-cores on VSC4 (Vienna Scientific Cluster 4) and in the most expensive simulation 512 cores. To evolve a typical simulation of the FDM halo with $N = 128$ on the base grid and 2 levels of refinement for 1000 timesteps running on 64 cores took about 380 cpu-hours. It used about 360 GB of memory. When simulating only the soliton we did not use refinement and thus the simulations were significantly "cheaper".

4 Soliton simulations

In this chapter we present the results of simulations of a point mass initially on circular orbit through an FDM soliton as shown in Figure 4.1. In the left picture the red dot shows the initial position of the test object in the FDM field. The right picture shows a snapshot from the simulation after 6000 timesteps and the orange curve shows the test objects path throughout the simulation. Initially the object had a velocity pointing towards the positive y-direction which is why the whole soliton and the particle together move with the center of mass into this direction through the simulation. In later parts we will use the center of mass of the system as the reference point to calculate the radial distance of the test object. An important thing to check initially is whether quantities like energy and mass are conserved during the simulations, which is done in the following section.

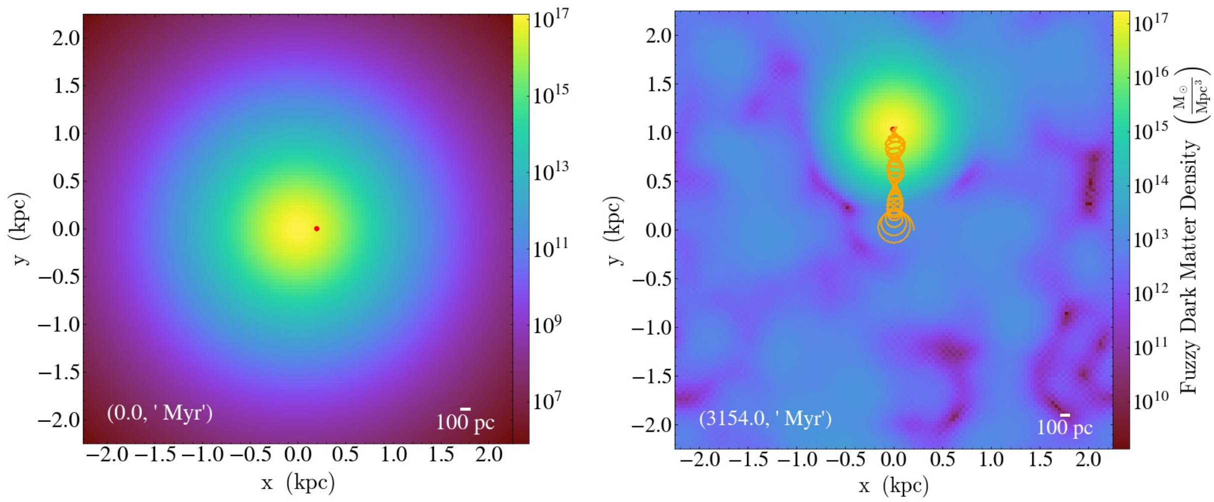

Figure 4.1: Left: A slice through the simulation box showing the value of the density of the FDM field initially with a test object shown in red. The object started on a circular orbit lying in the x-y plane with its initial velocity pointing in the y-direction. Right: Same as left but after 6000 timesteps. The orange line shows the trajectory of the test object throughout the simulation.

4.1 Conservation of energy and mass

As mentioned in more detail in section 1.8, the total energy E_{FDM} of the FDM field can be decomposed into three components denoted by V, K and Q. Meanwhile a massive test object (with mass m_t) will have the total energy $E_t(t)$ at time t that is the sum of its kinetic and potential energy, i.e.

$$E_t(t) = \frac{m_t}{2} v_t^2(t) + m_t \phi(t, \vec{x}). \tag{4.1}$$

Here we denoted the velocity of the test object as v_t and $\phi(t, \vec{x})$ is the gravitational potential at the position of the object. So in a simulation with one test object the energy of the entire system consisting of the object and the FDM field is supposed to be conserved over the duration of the simulation, i.e.:

$$\frac{d}{dt}E_{tot} = \frac{d}{dt}(V + K + Q + E_t) = 0 \tag{4.2}$$

Analogously, the total mass of the system consisting of the test object mass and the FDM field mass should be constant as well. This is a lot easier to check, because the mass of the test object is constant and is not exchanged with the field, so it only remains to see if the mass of the FDM field stays conserved. For a simulation on a grid with $N = 128$, $m_b = 10^{-21}$ eV, $M_c = 2.8 \cdot 10^6$ $\mathrm{M}_\odot$ and no massive particle these quantities are plotted in Figure 4.2. In Figure 4.3 the results of a simulation of the same soliton but with a test object with mass $m_t = 4.656 \cdot 10^5$ $\mathrm{M}_\odot$ are shown: Left the evolution of E_{FDM}, E_t and their sum E_{tot} is displayed and right the relative change of the total system energy $(E_{tot} - E_{tot}(t=0))/E_{tot}(t=0)$ is displayed right. It is clearly visible in the Figure that the FDM field and the test object exchanged energy during the simulation but the sum of their energies changes only by a couple of percent. Based on these results we conclude that the quantities mass and energy are well conserved during simulations with AxioNyx.

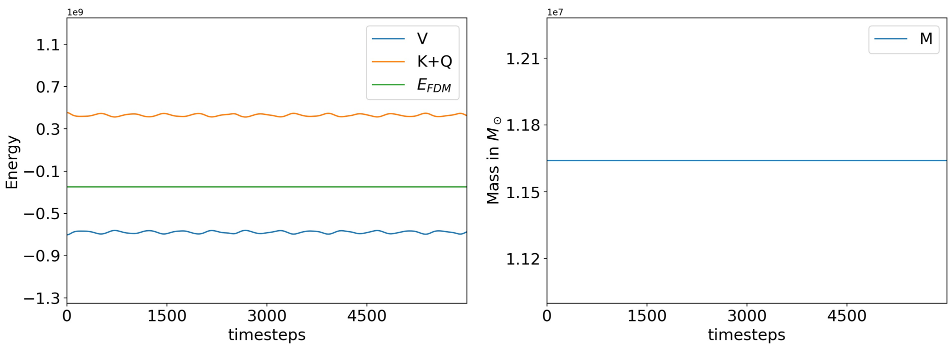

Figure 4.2: Left: Energy (in code units) of the FDM field and its components during a simulation including only a soliton with no test object. Right: Same as left panel but mass instead of energy.

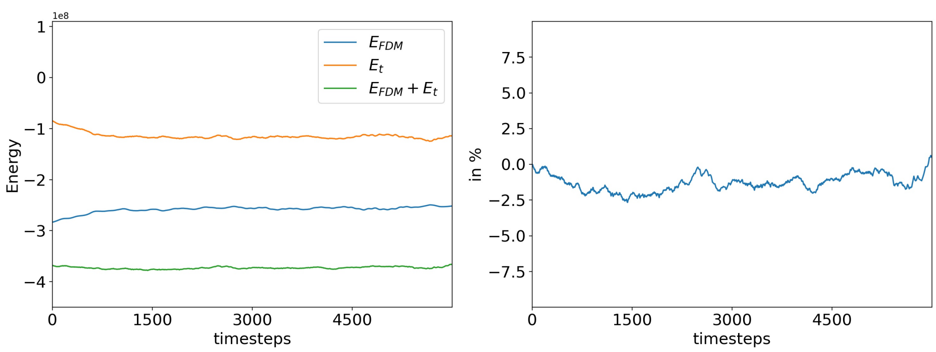

Figure 4.3: Left: Energy (in code units) of the FDM field and its components during a simulation including a soliton and a massive test object ($m_t = 4.656 \cdot 10^5$ $\mathrm{M}_\odot$). Right: Relative change in total energy E_{tot} for the same simulation.

4.2 Orbital decay

In Section 2.2 we discussed that due to dynamical friction it is expected that a test object moving on a circular orbit around a soliton should lose angular momentum and its orbit should decay i.e. the radial distance of the particle from the center of mass of the system should decrease. In the following we show results from simulations with a soliton configured to have $M_c = 2.8 \cdot 10^6$ $M_\odot$ and using a grid with $N = 128$. The simulation box has a length of 4.5 kpc and initially, the soliton is placed at the center of the box. Each simulation included a test object with a mass m_t which will be given as a fraction of the total soliton mass M_S ($M_S \approx 4M_c = 1.1 \cdot 10^7$ $M_\odot$).

In Figure 4.4 left one can see that massive test objects on initially circular orbit around a soliton indeed lose angular momentum as expected through the influence of dynamical friction and as expected more massive particles lose their angular momentum much faster. In Figure 4.4 right the trajectories of test objects from two separate simulations are plotted over each other in the center of mass frame and one can see that the more massive object inspirals towards the center.

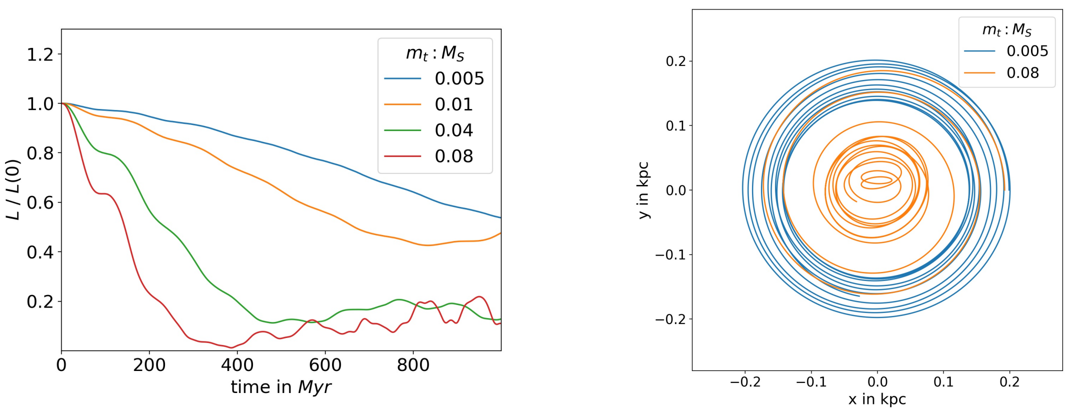

Figure 4.4: Left: Angular momentum L rescaled by initial angular momentum $L(0)$ of test objects initially in circular orbit around a soliton with different masses (given as fraction of the soliton mass M_S. Right: Trajectories after 1580 Myr of test objects from two simulations after about 1600 Myr with the same soliton but each time the particle has a different mass m_t given as a fraction of the soliton mass.

In Figure 4.5 one can see that the test objects do not sink uniformly towards the center but rather exhibit "stone skipping" trajectories which were also observed in simulations presented in [11]. The authors of [11] trace this behavior to the interaction between the test object and the soliton, which excites higher eigenmodes of the soliton. Just as seen in Figure 4.5 they also observed that for certain parameter choices the breathing mode reheats test objects orbiting at some distance from the center (see Figure 19 in [11]). According to the authors this effect is driven by the resonance between the soliton breathing mode and the orbital period. As seen in our Figure 4.5 in the right plot these effect is more significant for test objects with smaller masses, since dynamical friction is proportional to the object mass and therefore dominates in the case of massive test objects.

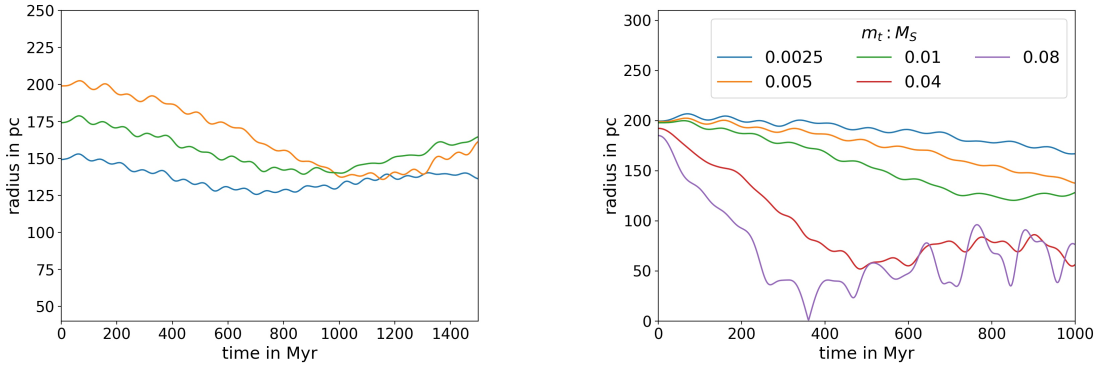

Figure 4.5: Left: Radial distance from the center of mass ("orbital radius") as a function of time for test objects with mass equal to 0.5% of the soliton mass M_S and different starting radii. Right: Radial distance as a function of time for test objects with different masses m_t but with the same initial conditions. The radial distance is calculated as distance to the center of mass of the soliton - test object system.

In Figure 4.6 one can see the orbital radii of the test objects in the simulations and for comparison the expected radius if only dynamical friction is considered as calculated by the formula (2.18). The left panel show results from three simulations with same initial position of the test object and different masses given as a fraction of the total soliton mass. In the right panel all particles have the same mass but they are placed at different initial distance from the center of the soliton. In all scenarios the inspiral is either slower than if only the friction were present or only observed initially and than even completely reversed.

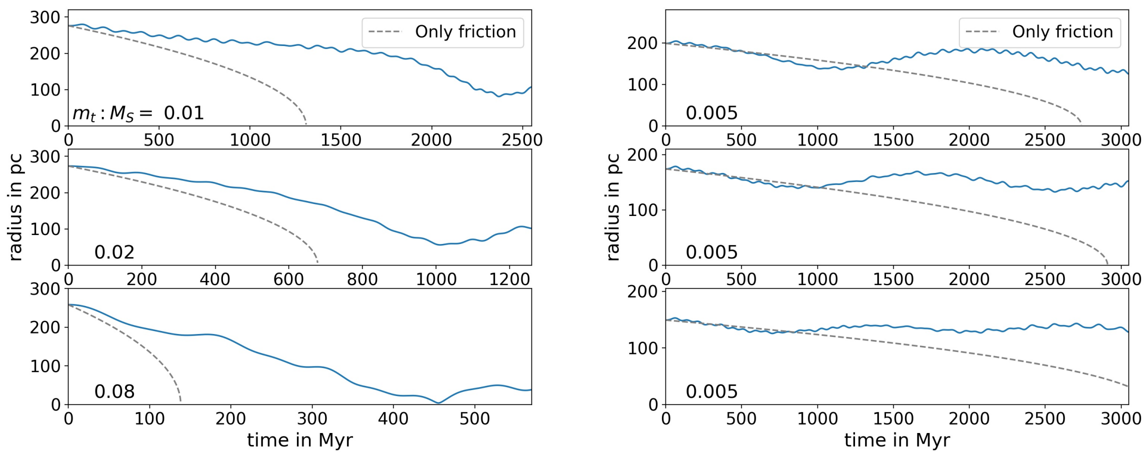

Figure 4.6: Left: Radial distance from center of mass of test objects in simulations with different masses given as fraction of the soliton mass. For comparison the dashed gray line is the radius calculated from equation (2.18), which estimates only the effects of dynamical friction. Right: Same as left but plot compares test objects with a different initial radius and the same mass.

4.2.1 Orbital lifetimes

From formula (2.13), one would expect that when keeping the initial radius r_i constant the orbital lifetime for test objects with different masses m_t should be inversely proportional to m_t. The results of multiple simulations plotted in Figure 4.7 are generally speaking in agreement with this prediction and seem to agree with (2.13). However note that in practice the test objects in most cases do not sink completely towards the center. Therefore we took the lifetime as the time it took for the test object to decay to about 1/3 of its initial radial distance. For light masses we observed "stone skipping" trajectories where the radius first decreased a bit but after some time it started increasing and reached its initial value. The two objects in the left plot in Figure 4.7 with masses corresponding to 0.5 % and 1 % of the soliton mass did not reach the decay criterion within the simulation which evolved the system for about 3300 Myr.

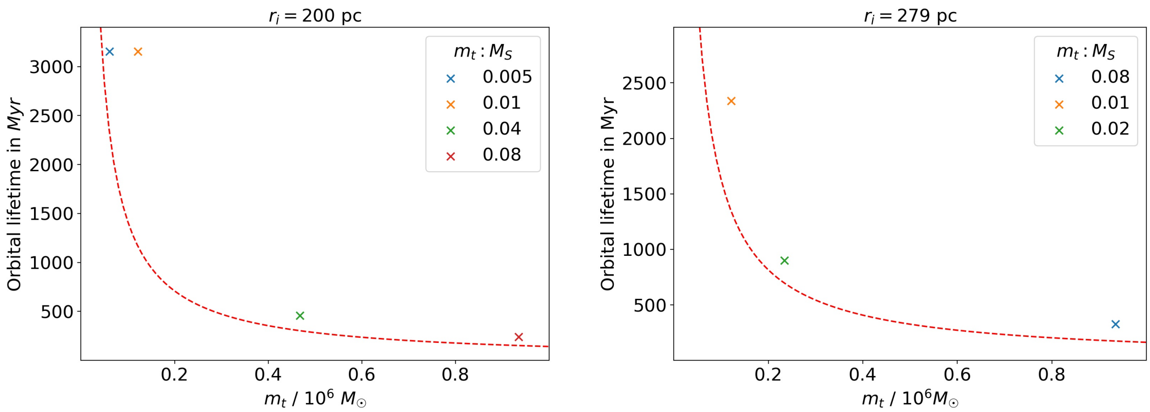

Figure 4.7: Orbital lifetime of test objects initially on circular orbits with different masses (given as percentage of total soliton mass). Note that the simulation ended after about 3300 Myr and the two masses which have this time as their lifetime did not decay from their original orbit within the simulation. Left: Initial radius $r_i = 200$ pc. Right: Initial radius $r_i = 279$ pc. Red line shows equation (2.13).

4.3 Solitonic Oscillations

To test Equation (1.30) we simulate a single soliton with resolution $N = 128$, $M_c = 2.8 \cdot 10^6$ M$_\odot$ and $m_b = 10^{-21}$ eV as the value for the mass of the FDM particle. From this simulation we plot the time dependence of the maximum value of the density (i.e. the "central" density) in Figure 4.8 left. One can see from the plot that the initial central density value drops in the first oscillation to about 90% of its initial value and then oscillates around a value of a little more than 92% of the initial value corresponding to about $1.27 \cdot 10^{17}$ M$_\odot$ Mpc^{-3}. The formula (1.30) gives 3.899 Gyr^{-1} as its oscillation frequency, which corresponds to a clear peak in the plot of the Fourier transform of the maximal density seen in Figure 4.8 right, so the solitonic oscillations found in our simulation are in good agreement with the formula (1.30).

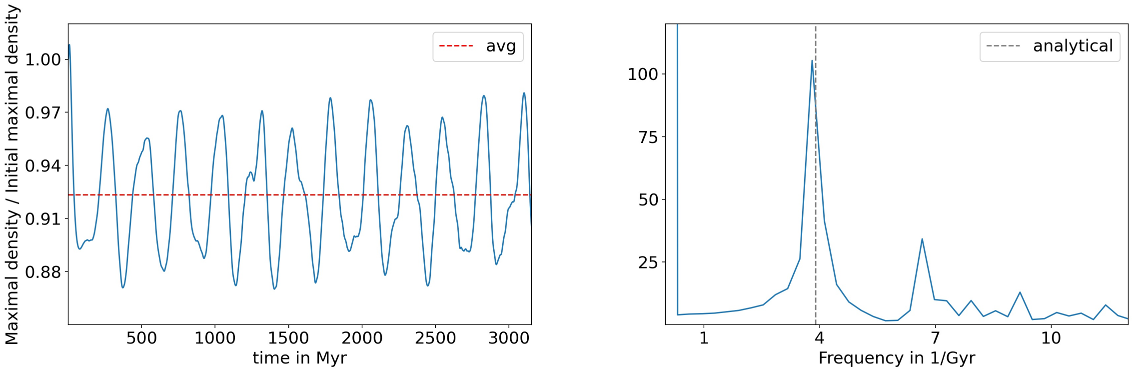

Figure 4.8: Left: Plot of the maximum density value of a soliton with initial values described in the text above. The red line shows the value around which the maximum density oscillates and this value was calculated by taking the average of the maximum density after discarding the first 30 % of the data, since initially there is an equilibration period. Right: Fourier transform of the maximum density shown in the left plot. The dashed line shows the value of the oscillation frequency calculated by formula (1.30). The difference between the peak frequency (3.8 Gyr^{-1}) and the analytical value (3.89 Gyr^{-1}) is less than 3 %. We also observe a second and third harmonic peak at higher frequencies.

Interestingly, when a massive particle orbits the soliton it interacts with it and also slightly changes its oscillation frequency. The way this happens seems to be that when a massive particle orbits the soliton near its center the mass contributes to the central potential well of the soliton and leads to the central density increasing which per formula (1.30) increases the oscillation frequency.

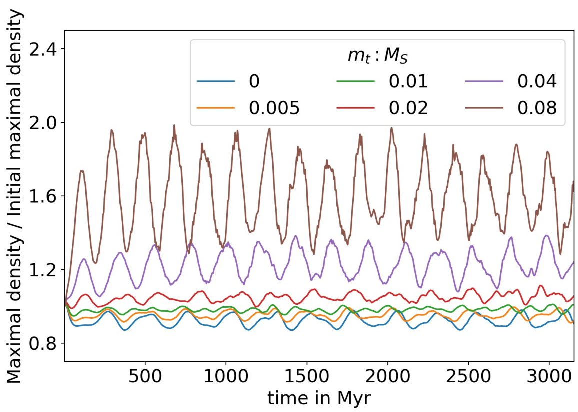

Figure 4.9: Oscillations of the maximal density (rescaled by its initial values) during multiple simulations with different test masses m_t given as percentage of the total soliton mass M_S.

To investigate this further see Figure 4.9, where the oscillations of maximum density are shown for systems with identical solitons ($M_c = 2.8 \cdot 10^6$ M$_\odot$), a point mass on circular orbits at initial radius of $r_i = 200$ pc. The point masses range from 0% to 8% of the total soliton mass M_S. It is clearly visible that the average maximum density around which the maximal density oscillates increases when the particle is more massive. This in turn leads to an increase in oscillation frequency as per formula (1.30), see Figure 4.10.

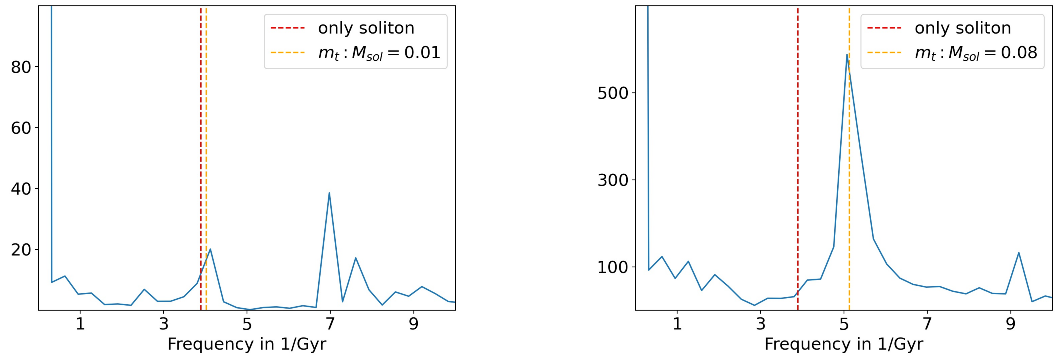

Figure 4.10: Left: Fourier transform of the maximum density for a soliton as described in text above with a massive particle in orbit at initial radius 200 pc and with 1% mass of the soliton. Red line indicates the initial frequency and the orange line indicates the frequency calculated by (1.30) with the average maximum density used for ρ_c. Right: The same as left panel but the test object has a mass corresponding to about 8% of the soliton mass.

5 FDM halo simulations

In this chapter we present the results of simulations of a point mass initially on circular orbit through an FDM halo constructed by the method described in section 3.3. In order to resolve the central region well enough but at the same time reduce the computational cost (e.g. cpu-time, memory) we used adaptive mesh refinement to increase our resolution in the vicinity of the most dense regions of the halos in the following simulations.

5.1 Simulation with $m_b = 5 \cdot 10^{-22}$ eV

Here we will present the results of simulations of an FDM halo which was set up using the procedure described in section 3.3 with the following parameters:

$$r_s = 5 \text{ kpc}, \qquad r_{\text{vir}} = 20 \text{ kpc}, \qquad M_{\text{vir}} = 2.825 \cdot 10^8 \text{ M}_\odot,$$
$$N_r = 215, \qquad m_b = 5 \cdot 10^{-22} \text{ eV}.$$

From these parameters we got $\rho_0 = 2.2 \cdot 10^5$ M$_\odot$/kpc^3, $N_p = 474$ and $r_c = 490$ pc. Furthermore, we used a grid (side length $L = 100$ kpc) with periodic boundary conditions and adaptive mesh refinement with 3 levels, where the first level had $N = 128$ cells and with each subsequent level the grid spacing gets decreased by a factor of 2.
Initially we let the FDM field evolve for 500 timesteps so that the field reaches a more relaxed state. In Figure 5.1 a slice through the simulation box is made and the density of the FDM field after the initial 500 timesteps is plotted left including the box of the subgrids with the refined regions and the density profile of the field is plotted right.

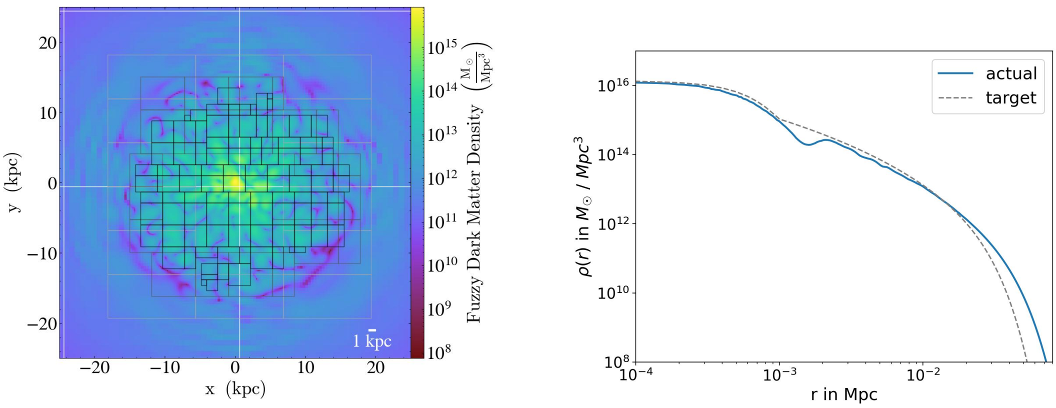

Figure 5.1: Left: FDM field in a simulation with the parameters described above after 500 timesteps. The grids indicate the refined regions. Right: The density profile of the FDM field from the snapshot shown left and the target density from the construction of the profile.

5.1.1 Estimating m_{eff} from a snapshot

We estimate m_{eff} from a snapshot of the simulation by identifying overdense regions in the FDM field, the so-called "granules". We approximate each granule as being spherical and estimate its radius. Then we take its density to be a constant value from a point approximately in the center and subtract the average density at the radial distance of the point from the center to get an "effective" density which we use to calculate the

approximate mass of the granule. Our estimate $\overline{m}_{\text{eff}}$ of m_{eff} is then the average over multiple granules and it can be seen as an order of magnitude estimate of m_{eff}.
In the above simulation we located 15 granules (see red points in Figure 5.2) and we got an estimate of $\overline{m}_{\text{eff}} \sim 4.2 \cdot 10^5$ M$_\odot$. In practice m_{eff} depends on the distance from the center of the halo and thus the estimated value which we found is appropriate to be compared with the average value for m_{eff} between 0 kpc and 9 kpc. When we use the formula (2.24)[3] and average over $r = 0 - 9$ kpc we get $8.11 \cdot 10^5$ M$_\odot$, which is about a factor of 2 different than our rough estimate of $\overline{m}_{\text{eff}}$ from the snapshot.

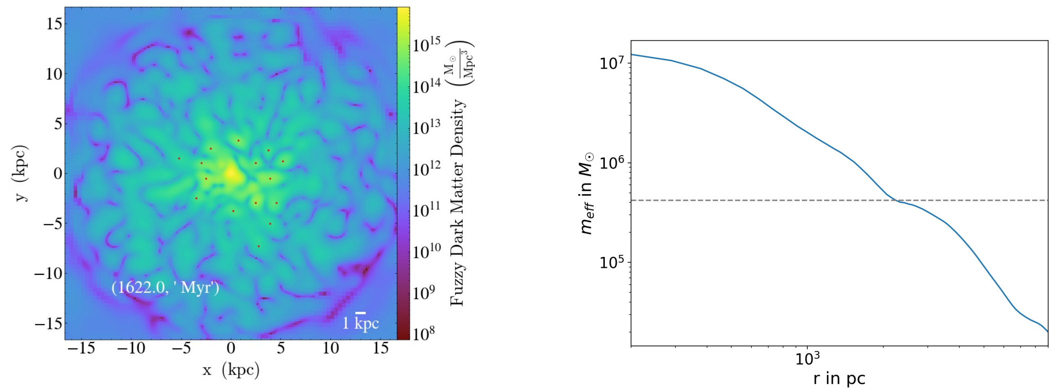

Figure 5.2: Left: The red dots indicate which granules were chosen to estimate m_{eff} by the process described above. Right: m_{eff} calculated from (2.24) for the FDM halo from the simulation shown left. The dashed line indicates the estimated value $\overline{m}_{\text{eff}}$ representing an order of magnitude estimate as described in this section.

5.1.2 Relaxation

Using the estimate for m_{eff} from the previous section we can apply the theory from section 2.3 regarding relaxation. One prediction (e.g. from formula (2.29)) is that when the ratio $\mu_{\text{eff}} > 1$ then dynamical friction ("cooling") is the dominant effect on a test object, while for $\mu_{\text{eff}} < 1$ it is negligible and the stochastic density fluctuations (diffusion) are dominating.

To test this we ran two simulations, one with $m_t = 10^7$ M$_\odot$ (initially $\mu_{\text{eff}} \sim 10$) and the second one with $m_t = 1000$ M$_\odot$ (initially $\mu_{\text{eff}} \sim 0.001$) and the trajectories of the test objects in the center of mass frame are shown in the Figure 5.3. Both objects started with the same initial position and velocities set up such that the masses are on circular orbits lying in the x-y plane. From the x-y projection it is clearly visible that the more massive object inspirals towards the center as expected due to dynamical friction. The x-z projection shows interestingly that both trajectories are not planar during the simulation but rather the test objects also change their z component. This can be explained through the effect of the stochastic density fluctuations which are present in all 3 directions and thus can cause the objects to move out of the original plane of motion. This is in agreement with the observation that the trajectory of the more massive object gets less deflected in the z direction and the less massive object got more deflected in the z direction. Meanwhile Figures 5.4 and 5.5 show the radii from the simulations in the left plots and μ_{eff} as a function of the radius calculated from (2.24) in the right plot.

[3]the used value for σ can be found in Appendix B in the description of Figure 6.2

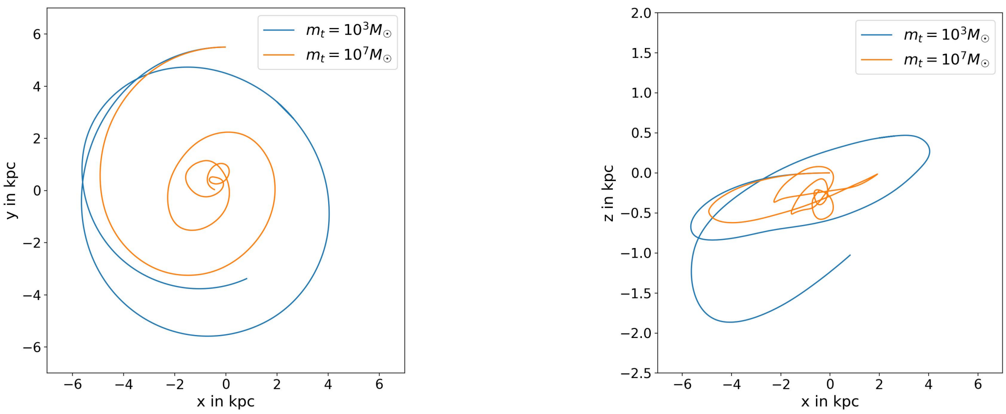

Figure 5.3: Left: Trajectories during the first 5740 Myr of two test objects through the x-y plane in a FDM field with different masses m_t and consequently μ_{eff}. The heavier particle with the higher μ_{eff} inspirals due to dynamical friction within its first orbit rapidly towards the center, where it stops inspiraling and due to random density fluctuations it experiences the "heating" effect. Meanwhile the lighter particle with low μ_{eff} stays on an elliptical orbit. Right: Same for the x-z plane.

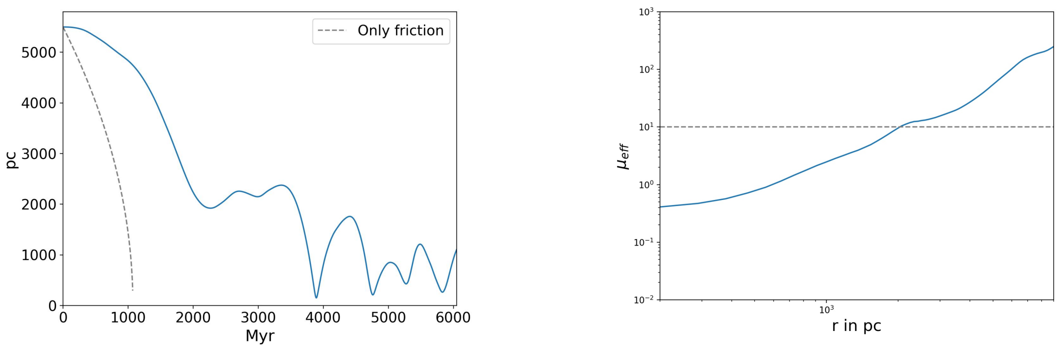

Figure 5.4: Left: Orbital radius of a heavy test mass with $m_t = 10^7$ $M_\odot$ (initially $\mu_{\text{eff}} \sim 10$). The gray line is the radius calculated by the approximate formula (2.18), which takes only dynamical friction into account. Right: μ_{eff} calculated using Formula (2.24) (the value for σ is given in the description of Figure 6.2) The dashed line is plotted at $\mu_{\text{eff}} = 10$ and below the line is the region in which dynamical friction becomes less and less relevant. The lines intercept at about 2065 pc. $\mu_{\text{eff}} = 1$ at about 650 pc, which is approximately the value one gets from (2.34) for the stalling radius and the test object seems indeed to oscillate around this value towards the end of the simulation.

From the plots in Figure 5.4 we can see clearly that as predicted the heavy test object does initially sink from the initial separation of about 5500 pc fast towards the center due to dynamical friction but as it gets to about 2200 pc the orbital decay slows down and after a couple more elliptical orbits the test object seems to stop decaying towards the center and instead orbits at a mean distances of about 1000 pc.

Meanwhile the light test object with 10^3 $M_\odot$ stays on an elliptical orbit which ranges between 6000 pc and 4000 pc during the simulation, which confirms that dynamical friction is not the dominant effect for this parameter choice during the time frame of the simulation.

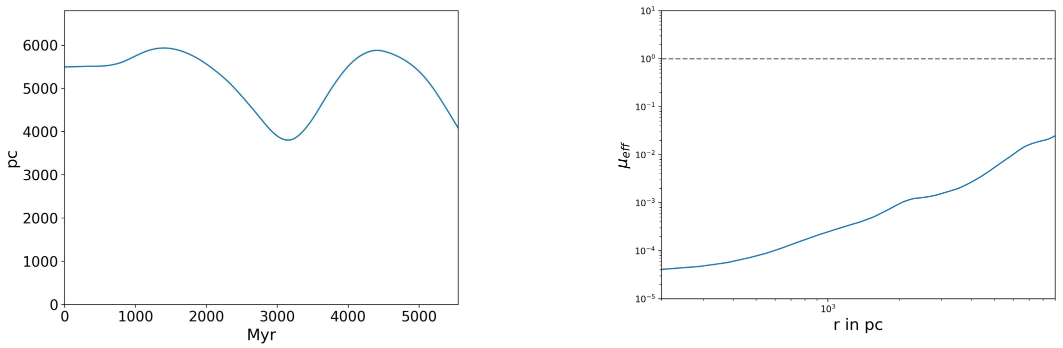

Figure 5.5: Left: Same plot as in Figure 5.4 but with $m_t = 10^3$ $M_\odot$ (initially $\mu_{\text{eff}} \sim 0.001$). Rigth: Same as in Figure 5.4 but this time the dashed line is plotted at $\mu_{\text{eff}} = 1$. During the simulation μ_{eff} stay well below the line, indicating that dynamical friction is negligible.

To examine more scenarios where the stochastic density fluctuations should be dominating over the dynamical friction we conducted two more simulations but placed the test object closer to the halo core. In one simulation we placed an object with mass $m_t = 10^5$ $M_\odot$ on a circular orbit at an initial distance of 2500 pc from the center and in the second one at 3000 pc with $m_t = 5 \cdot 10^5$ $M_\odot$. In Figure 5.6 the trajectories from these simulations are plotted in the center of mass frame. In this case one can see in the x-y projection that the test objects do not inspiral rapidly towards the center but rather stay on elliptical orbits while the x-z projection clearly shows that both objects get heavily perturbed in the z direction due to the influence of stochastic density fluctuations. Figure 5.7 depicts the orbital radii during these simulations. In Figure 5.8 the test object energy E_t and its components are plotted as a function of time and in both these cases E_t does increase over the course of the simulation, meaning the objects gained energy from the FDM field.

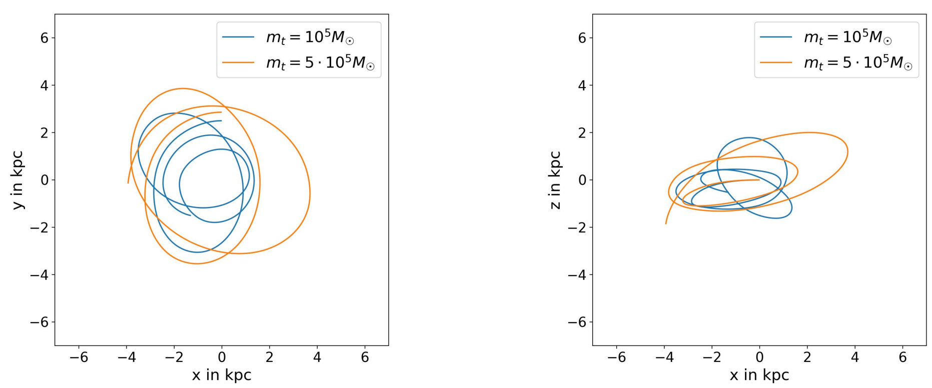

Figure 5.6: Left: Trajectories of two test objects after about 5850 Myr through the x-y plane in a FDM field. Right: Same but x-z plane.

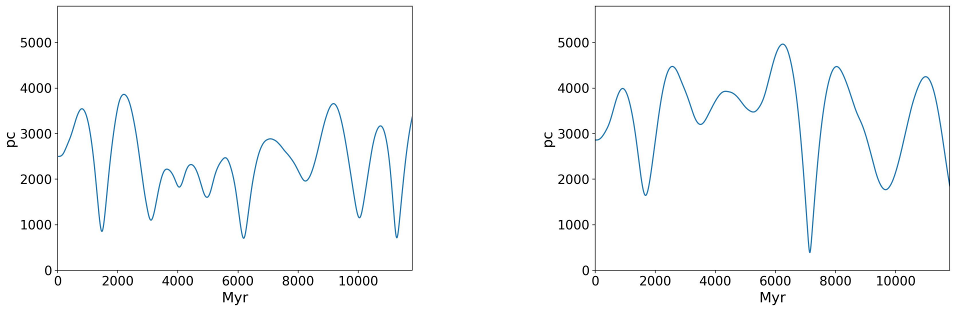

Figure 5.7: Left: Orbital radius of the test object with $m_t = 10^5$ M$_\odot$. $\mu_{\text{eff}} = 1$ at about 6000 pc. Right: Same as left but $m_t = 5 \cdot 10^5$ M$_\odot$ and in this case $\mu_{\text{eff}} = 1$ at about 3600 pc.

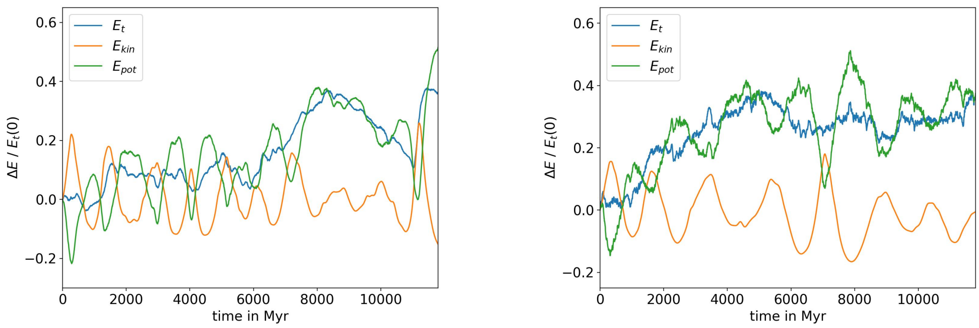

Figure 5.8: Left: Change in energy E_t (calculated as $\Delta E_t = E_t(t) - E_t(0)$ and given in units of $E_t(0)$) of the test object with mass $m_t = 10^5$ M$_\odot$. Rigth: Same as left but $m_t = 5 \cdot 10^5$ M$_\odot$.

5.2 Simulation with $m_b = 7.5 \cdot 10^{-22}$ eV

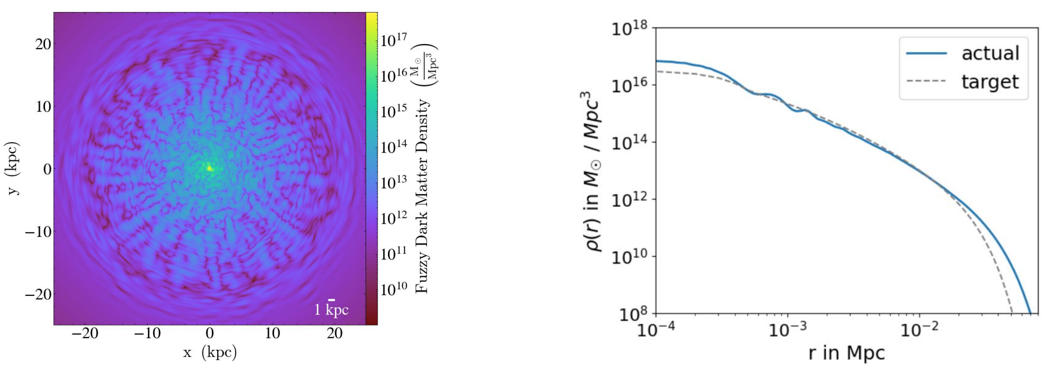

Figure 5.9: Left: FDM field in a simulation with parameters described in this section after 500 timesteps. Right: The initial density profile of the FDM field from the simulation and the target density from the construction of the profile.

Similarly to the simulation in the previous section we set up another simulation but this time for a different FDM particle mass $m_b = 7.5 \cdot 10^{-22}$ eV.

The FDM halo was set up with the following parameters:

$$r_s = 2 \text{ kpc}, \qquad r_{\text{vir}} = 20 \text{ kpc}, \qquad M_{\text{vir}} = 2.825 \cdot 10^8 \text{ M}_\odot$$
$$N_r = 416 \qquad m_b = 7.5 \cdot 10^{-22} \text{ eV}.$$

From these parameters we got $\rho_0 = 1.89 \cdot 10^6 \text{M}_\odot/\text{kpc}^3$, $N_p = 1036$ and $r_c = 325$ pc. Once again we used a grid (side length $L = 100$ kpc) with periodic boundary conditions and adaptive mesh refinement with 3 levels, but in this case the first level had $N = 256$ cells and with each subsequent level the grid spacing gets decreased by a factor of 2. We chose a higher resolution because the size of the granules is inversely proportional to m_b.

Again first we let the FDM field evolve for 500 timesteps so that the field reaches a more relaxed state and in Figure 5.9 a slice through the simulation box is made. The density of the FDM field after the initial 500 timesteps is plotted left while the density profile of the field is plotted right.

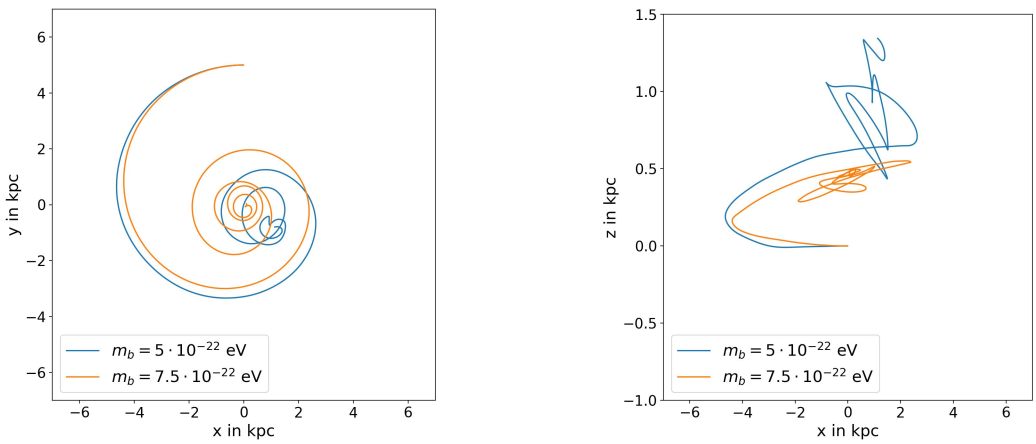

Figure 5.10: Left: The trajectory in the $x-y$ plane after 3900 Myr of a test object in the center of mass frame from the simulation described in this section in orange and in blue the trajectory of the test object with the same mass ($m_t = 10^7$ M$_\odot$) from the previous section. Right: The same but for $x - z$ plane.

Next we performed a simulation with a test object of mass $m_t = 10^7$ M$_\odot$ and for comparison plotted the trajectory of the test object in the center of mass frame together with the trajectory of a test object from an identical simulation with only $m_b = 5 \cdot 10^{-22}$ eV in Figure 5.10. This was done to directly compare the effect of different FDM boson mass m_b and as seen in the figures a higher m_b leads to faster inspiral and smaller effects (e.g. less deflected into the z direction) from the granules. This comes from the fact that the granule effective mass is proportional to $1/m_b^3$, i.e. it gets smaller for higher m_b. Thus for higher m_b diffusion plays a smaller role and dynamical friction is more impactful. Because of this for higher m_b the point mass inspirals closer to the center before the granules are massive enough to counter dynamical friction and stall the orbital decay. The radii are shown in Figure 5.11, where with the dashed lines the stalling radii are also plotted (radius where $\mu_{\text{eff}} = 1$). Both objects do not go below their respective dashed line and stay close to the line in distances where μ_{eff} is less than 10.

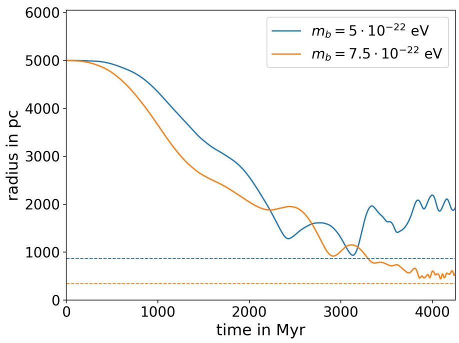

Figure 5.11: The orbital radius a test object of mass $m_t = 10^7$ $M_\odot$ in two simulations with different m_b. The blue (≈ 870 pc) and orange (≈ 350 pc) dashed lines indicate the radii at which $\mu_{\rm eff} = 1$ (i.e. the theoretical stalling radius). The inspiral does indeed stall and the objects never go below the stalling radii during the simulations but stabilise their orbits at distances larger by about a factor 2. For comparison the core radii r_c are: 490 pc (blue) and 325 pc (orange).

5.2.1 Deflection into the perpendicular direction

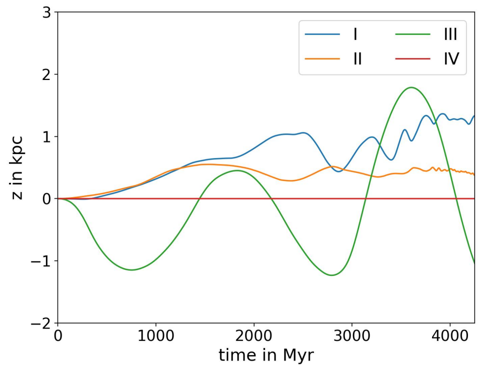

Figure 5.12: The z coordinate (coordinate perpendicular to the original plane of orbit) value from different simulations plotted as a function of time. The line IV is from a simulation where the FDM field consists only of a soliton and thus there are no stochastic density fluctuations ("granules") and the orbit stays planar. The lines I, II and III are from previously shown simulations containing an FDM halo with the following parameters: I: $m_b = 5 \cdot 10^{-22}$ eV$, m_t = 10^7$ $M_\odot$, $r_i = 5$ kpc, II: $m_b = 7.5 \cdot 10^{-22}$ eV, $m_t = 10^7$ $M_\odot, r_i = 5$ kpc and III: $m_b = 5 \cdot 10^{-22}$ eV, $r_i = 2.5$ kpc and $m_t = 10^5$ $M_\odot$. This deflection is caused by the granules which are stronger when m_b is smaller and have a bigger impact on less massive test objects and objects closer to the center.

In the simulations with a test mass orbiting through an FDM halo we observed that the orbits got deflected into the direction perpendicular to the initial plane of motion. In our simulation the initial plane of motion is the x-y plane and the perpendicular direction is the z direction. To compare how strong this deflection was in different simulations we plotted in Figure 5.12 the value of the z coordinate of the test mass (initial value is 0, the coordinates systems are placed such that initially all test object are placed at a point with coordinates $(0, y(0), 0)$). II is from the simulation with halo parameters described in section 5.2 where $m_b = 7.5 \cdot 10^{-22}$ eV and a mass $m_t = 10^7$ M$_\odot$ was placed at an initial distance from the center of the box at $r_i = 5$ kpc. I has the same parameters as II except $m_b = 5 \cdot 10^{-22}$ eV (I and II are the simulations from Figure 5.10). These two inspiral after a couple 1000 Myr relatively close to the core which performs a random walk in the central region of the halo and one can see after about 3000 Myr the effects coming from this stochastic motion of the core. III is from the simulation with parameters given in section 5.1 with $r_i = 2.5$ kpc and $m_t = 10^5$ M$_\odot$. IV is from a simulation where the FDM field consists only of a soliton with simulation parameters given in 4.2 and is included in the plot to showcase that there is no deflection into the z-direction in this case since there are no density fluctuations inside a soliton.

6 Summary and Conclusion

The purpose of this work was to understand how massive objects move in an FDM halo. The studied scenarios which included very massive test objects apply to the physical scenario of a supermassive black hole orbiting within a galactic halo. Meanwhile less massive test objects may represent stars, for which only the "heating" effect (diffusion) is relevant. In the following we sum up the main results and conclusion from the previous sections.

In Section 4 we show simulations of a test object orbiting through an FDM soliton core and observed dynamical friction which causes the test object to inspiral. For light objects with masses that were not more than 1% of the soliton mass the trajectories were not monotonically decreasing in radius. Instead, due to resonance with the solitonic oscillations some test objects were on "stone skipping" trajectories which was previously observed in [11]. As expected from the dynamical friction theory more massive test objects had stronger dynamical friction and inspiraled towards the center. This happens because a heavier "wake" forms behind test objects with higher masses. We also calculated the frequency of the solitonic oscillations by performing the Fourier transform of the highest density amplitude with time. The peak of the frequency of the solitonic oscillations agreed with the analytical value calculated with the formula given in the literature, i.e. the difference was less than 3 %. Moreover, we find that the presence of a massive object increases the soliton oscillation frequency. This happens because massive objects contribute to the central gravitational potential, which in turn increases the density in the center of the soliton.

In the second part of this work we performed simulations of a test object orbiting through an FDM halo which due to the interference between excited states has stochastic density fluctuations ("granules"). As expected from theory we observed that for higher m_b (the FDM particle mass) the granules were smaller. We confirmed the order of magnitude of the theoretical value for the effective mass m_{eff} of the granules in a simulation, which is an important quantity to compute the relaxation effects. In Appendix B we examined the velocity distribution function of the FDM field in our simulations and found that its shape is well approximated as Maxwellian and showed the FDM halo density profile outside the core is well approximated by the isothermal sphere profile. The Maxwellian distribution function and the isothermal sphere profile were used as approximations in the theoretical derivations by other authors.

We find that more massive objects inspiral faster and get closer to the center due to dynamical friction but stop inspiraling at distances consistent with the theoretical predictions for the stalling radius. For less massive point masses the effects of the stochastic density fluctuations were more relevant and perturbed the orbit significantly. We noticed that the orbits did not stay in their original plane but got distorted into the perpendicular direction (in our case z-direction) which was due to the stochastic density fluctuations and thus more profound for less massive objects and objects closer to the center of the halo. Once a test object inspirals close enough to the solitonic core of the FDM halo we observed that the orbit got disturbed by the random walk of the solitonic core.

Appendix A: Friction coefficient $C(kr)$ for small kr

We start with the equation for the friction coefficient C given in (2.8). To get an approximation for small kr (i.e. $kr \ll 1$) let us calculate the Taylor series up to the 2nd order around 0:

$$C \approx C(0) + C'(0)(kr) + \frac{1}{2}C''(0)(kr)^2 \tag{6.1}$$

$C(0) = 0$ since $Cin(0) = 0$ and $\sin(kr)/(kr) = 1$ at $kr = 0$. Next let us calculate the first derivative:

$$C'(kr) = \frac{1-\cos(2kr)}{(2kr)} + \frac{\cos(2kr)}{kr} - \frac{\sin(2kr)}{2(kr)^2} \tag{6.2}$$

This expression needs to be carefully evaluated at $kr = 0$ using l'Hopital's rule for limits, but if done properly one gets $C'(0) = 0$. This result is also obvious from looking at the plot of C in the left panel of Figure 6.1, since there is a minimum at $kr = 0$. The proper calculation of C'' is tedious, so instead one can verify graphically that $C''(0) = \frac{2}{3}$ in the right panel of Figure 6.1. With that one finds for $kr \ll 1$:

$$C \approx \frac{1}{2}\frac{2}{3}(kr)^2 = \frac{1}{3}(kr)^2. \tag{6.3}$$

To see a comparison between the value from this approximation and the exact value calculated numerically see the figure below.

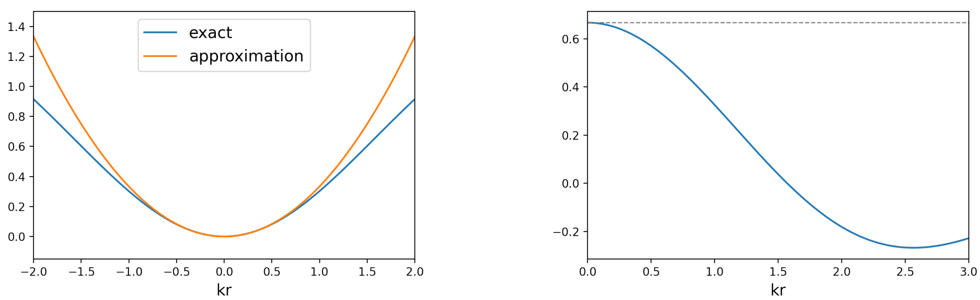

Figure 6.1: Left: Blue: $C(kr)$ calculated using (2.8) (the integral was evaluated numerically). Orange: the value from the approximation $C = \frac{1}{3}(kr)^2$. Right: Numerically calculated second derivative of C. The dashed gray line is at $y = 2/3$.

Appendix B: Velocity distribution functions

Assuming the velocity distribution of the FDM field is “Maxwellian”, i.e. of the form

$$f(\vec{v}) = \frac{1}{(2\pi\sigma^2)^{3/2}} e^{-v^2/(2\sigma^2)} \tag{6.4}$$

then the speed $v = |\vec{v}|$ has the distribution $f(v)$:

$$f(v) = \frac{1}{(2\pi\sigma^2)^{3/2}} 4\pi v^2 e^{-v^2/(2\sigma^2)}. \tag{6.5}$$

To compute the velocity distribution function from a snapshot of a simulation we used the relation

$$f(\vec{v}) = \frac{1}{N} \left| \int d^3x \exp\left[-im\vec{v}\vec{x}/\hbar\right] \psi(x) \right|^2 \tag{6.6}$$

with N being a normalization factor. We used (6.5) to fit the resulting velocity distribution functions from snapshots of simulations and in Figure 6.2 such fits for 3 different simulations are shown. The left panel is from a simulation having a soliton only (parameters as described in 4.2) while the central and right panel are from simulations with FDM halos (as described in section 5.1 and 5.2). One can see that (6.5) seems to be a reasonable approximation to the actual velocity distribution functions.

The isothermal sphere density has been widely used as an approximation in the literature as well as in this thesis. Since we have determined the velocity distribution functions of the fields in our simulations we can use them to determine the values of σ. Using these values we can compare how accurate this approximation is. In Figure 6.3 we compare the density profile from a simulation with the profile from (2.16) using the fitted values for σ. Again the left panel is for a soliton while the central and right panel are from simulations containing FDM halos. One can see that for the FDM halos the isothermal sphere is a reasonable approximation of the actual density profile for a wide range of radii and becomes inaccurate only close to the center and in the region far from the center once the exponential term starts to suppress the NFW profile.

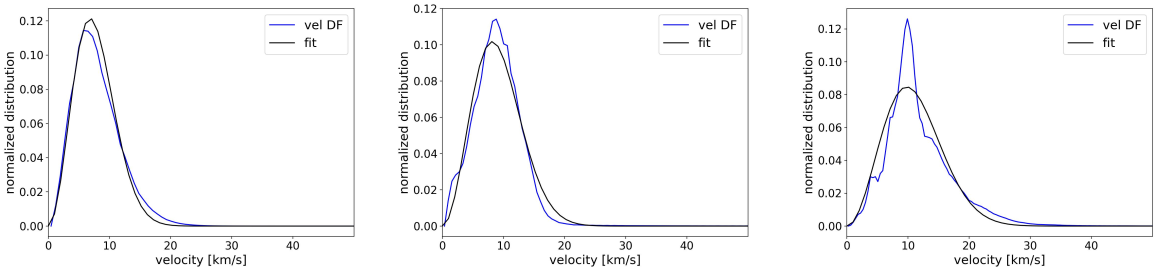

Figure 6.2: Normalized velocity spectra (blue) fitted with (6.5) (black) from simulations containing: Left: a soliton with parameters given in 4.2 (fit: $\sigma = 4.83$ km/s). Center: an FDM halo with parameters given in 5.2 (fit: $\sigma = 6.93$ km/s). Right: an FDM halo with parameters given in section 5.1 (fit: $\sigma = 5.77$ km/s).

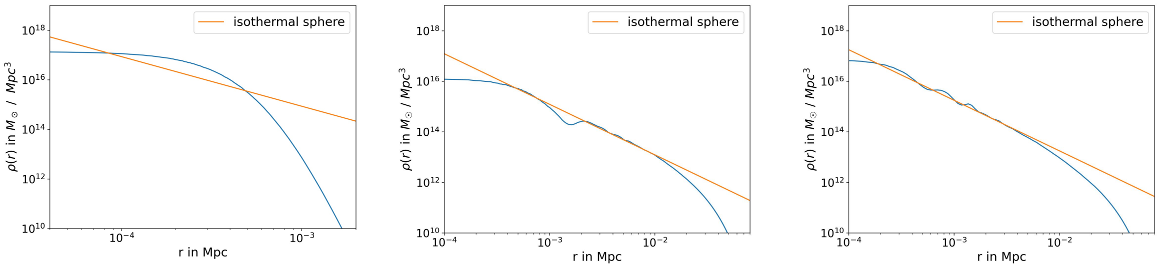

Figure 6.3: Isothermal sphere profile (2.16) in orange compared with density profile of the FDM field (in blue) from simulations containing: Left: a soliton with parameters given in 4.2. Center: an FDM halo with parameters given in section 5.2. Right: an FDM halo with parameters given in 5.1. The values used for σ are given in the description of Figure 6.2.

References

[1] Planck Collaboration (2020). *Planck 2018 results. VI. Cosmological parameters* Astronomy Astrophysics, 641, A6

[2] Planck Collaboration (2016). *Planck 2015 results. XIII. Cosmological parameters* Astronomy Astrophysics, Volume 594, A13

[3] Dodelson S., Schmidt F. (2021). *Modern Cosmology*, Academic Press

[4] Rubin V., Ford W. K. Jr., Thonnard N. (1980). *Rotational properties of 21 SC galaxies with a large range of luminosities and radii, from NGC 4605 (R=4kpc) to UGC 2885 (R=122kpc).* The Astrophysical Journal, 238:471-487

[5] Schive H., Chiueh T., Broadhurst T. (2014). *Cosmic Structure as the Quantum Interference of a Coherent Dark Wave*, Nature Phys 10, 496–499

[6] Hu W.,Barkana R., Gruzinov A. (2000). *Fuzzy Cold Dark Matter: The Wave Properties of Ultralight Particles*, Phys. Rev. Lett. 85, 1158

[7] Marsh D. (2016). *Axion Cosmology* Physics Reports, Volume 643, Pages 1-79, ISSN 0370-1573

[8] Milosavljevic M., Merritt D. (2003). *Long Term Evolution of Massive Black Hole Binaries*. Astrophys. J. 596

[9] Hui L., Ostriker J., Tremaine S., Witten E. (2017). *Ultralight scalars as cosmological dark matter*, Phys. Rev. D 95, 043541

[10] Bar-Or B., Fouvry J., Tremaine S. (2019). *Relaxation in a Fuzzy Dark Matter Halo*, The Astrophysical Journal, 871:28

[11] Wang Y., Easther R. (2022). *Dynamical Friction From Ultralight Dark Matter*, Phys. Rev. D 105, 063523

[12] Niemeyer J. (2019). *Small-scale structure of fuzzy and axion-like dark matter*, Progress in Particle and Nuclear Physics, Volume 113, 2020, 103787, ISSN 0146-6410

[13] Edwards F., Kendall E., Hotchkiss S., Easther R. (2018). *PyUltraLight: A Pseudo-Spectral Solver for Ultralight Dark Matter Dynamics*, Journal of Cosmology and Astroparticle Physics, Volume 2018

[14] Schive H., Chiueh T., Broadhurst T. (2020). *Soliton Random Walk and the Cluster-Stripping Problem in Ultralight Dark Matter*, Phys. Rev. Lett. 124, 201301

[15] Li X., Hui L., Yavetz T. (2021). *Oscillations and random walk of the soliton core in a fuzzy dark matter halo*, Phys. Rev. D 103, 023508

[16] Schive H., Liao M., Woo T., Wong S., Chiueh T., Broadhurst T., Hwang W-Y. (2014). *Understanding the Core-Halo Relation of Quantum Wave Dark Matter, DM, from 3D Simulations*, Phys. Rev. Lett. 113, 261302

[17] Navarro J. F., Frenk C. S., and White S. D. M. (1996). *The Structure of cold dark matter halos*. Astrophys. J., 462:563–575

[18] Navarro J. F., Frenk C. S., and White S. D. M. (1997). *A Universal density profile from hierarchical clustering*. Astrophys. J., 490:493–508

[19] Lora V., Magana J., Bernal A., Sanchez-Salcedo F. J., Grebel E. K. (2012). *On the mass of ultra-light bosonic dark matter from galactic dynamics*. Journal of Cosmology and Astroparticle Physics, Volume 2012, February 2012

[20] Bozek B.,Marsh D., Silk J., Wyse R. (2015). *Galaxy UV-luminosity function and reionization constraints on axion dark matter*. Monthly Notices of the Royal Astronomical Society, Volume 450, Issue 1, 11 June 2015, Pages 209–222

[21] R. J. Bouwens et al (2015). *UV Luminosity Functions at redshifts z 4 to z 10: 10000 Galaxies from HST Legacy Fields*. ApJ 803 34

[22] Dentler M., Marsh D., Hložek R., Laguë A., Rogers K., Grin D. (2022). *Fuzzy Dark Matter and the Dark Energy Survey Year 1 Data*, Monthly Notices of the Royal Astronomical Society, Volume 515, Issue 4, October 2022, Pages 5646–5664

[23] Rogers K., Peiris H. (2021). *Strong bound on canonical ultra-light axion dark matter from the Lyman-alpha forest*. Phys. Rev. Lett. 126, 071302

[24] Dalal N., Kravtsov A. (2022). *Not so fuzzy: excluding FDM with sizes and stellar kinematics of ultra-faint dwarf galaxies*. Phys. Rev. D 106, 063517

[25] Binney J., Tremaine S. (2008). *Galactic Dynamics*. Princeton University Press, 2nd Edition

[26] Chandrasekhar S. (1943). *Dynamical Friction. I. General Considerations: the Coefficient of Dynamical Friction*. Astrophysical Journal, vol. 97, p.255

[27] Weinberg S. (2015). *Lectures on Quantum Mechanics*. Cambridge University Press, 2nd Edition

[28] Goerdt T., Moore B., Read J., Stadel J., Zemp M. (2006). *Does the Fornax dwarf spheroidal have a central cusp or core?*. Monthly Notices of the Royal Astronomical Society, 368: 1073-1077

[29] Schwabe B., M. Gosenca, Behrens C., Niemeyer J. C., Easther R. (2020). *AxioNyx: Simulating Mixed Fuzzy and Cold Dark Matter*. Phys. Rev. D 102, 083518

[30] Almgren A. S., Bell J. B., Lijewski M.J., Lukic Z., Van Andel E. (2013). *Nyx: A Massively Parallel AMR Code for Computational Cosmology*. Astrophysical Journal, 765, 39

[31] Schwabe B., Niemeyer J., Engels J. (2017). *Simulations of solitonic core mergers in ultra-light axion dark matter cosmologies*, Phys. Rev. D 94, 043513

[32] Yavetz T., Li X., Hui L. (2021). *Construction of Wave Dark Matter Halos: Numerical Algorithm and Analytical Constraints*, Phys. Rev. D 105, 023512

[33] Zagorac J., Sands I., Padmanabhan N., Easther R. (2021). *Schrödinger-Poisson Solitons: Perturbation Theory*, Phys. Rev. D 105, 103506